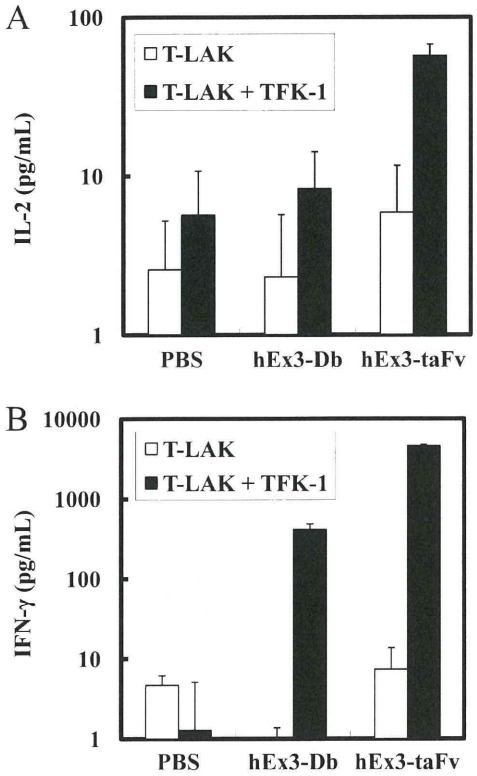

FIGURE 4. **Cytokine production by T-LAK cells mediated by BsAbs.** Concentration of IL-2 (*A*) and IFN-γ (*B*) were evaluated using ELISA.

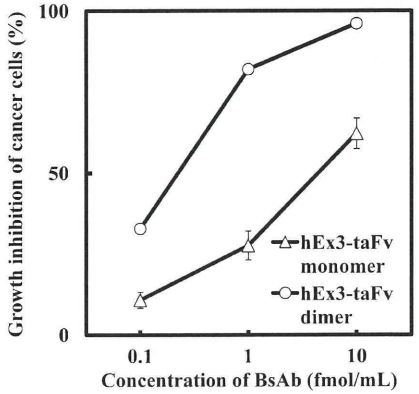

FIGURE 5. **Growth inhibition of EGFR-positive TFK-1 cells by the monomeric and dimeric fractions of hEx3-taFv.** The hEx3-taFv and T-LAK cells were added to TFK-1 cells at a ratio of 5:1. Data are presented as the mean value ± S.D. and are representative of at least three independent experiments with similar results.

ization on the inhibition of human carcinoma cell growth, we compared fractionated hEx3-taFv monomer with the dimer by MTS assay. The hEx3-taFv dimer showed a more intense effect than the monomer and strongly inhibited the growth of TFK-1 cells even at a concentration of 1 fmol/ml (Fig. 5). Thus, multimerization can also lead to increases in the functionality of hEx3-taFv.

Preparation and Analyses of Covalently Linked hEx3-taFv Dimer—Multimerization can increase the effectiveness of small BsAbs, but it raises a concern about dissociation to the monomer form, especially at low concentrations, such as those found after *in vivo* administration. To produce a covalently linked hEx3-taFv dimer, we designed hEx3-taFv′-3C-Fc, in which an HRV3C protease recognition site was inserted between the hinge region and the Fc portion (Fig. 6*A*). In a manner similar to that used for hEx3-taFv, hEx3-$(taFv')_2$ was prepared, and its covalently linked form was confirmed by SDS-PAGE analysis under reducing and nonreducing conditions. In the MTS assay, hEx3-$(taFv')_2$ showed intense growth inhibition effects not only to the hEx3-taFv dimer but also to hEx3-taFv-3C-Fc (Fig. 6, *B* and *C*). From these results, we concluded that the tandem scFv is the most effective format for hEx3, and its function can be enhanced further by dimerization.

DISCUSSION

In the present study, we converted the format of hEx3-Db, a humanized diabody targeting EGFR and CD3, into taFv to examine the influence of small BsAb formats on their function using cytotoxicity assays, SPR imaging, isothermal titration calorimetry, and flow cytometry.

Although in most cases, Dbs can be expressed in soluble form in bacteria, taFv are often difficult to express in bacteria because of the formation of aggregates. Hence, refolding techniques or mammalian expression systems are routinely used to produce soluble taFv (25, 26). Researchers have engineered linker length (27, 28) and optimized linkers using phage display technology (15) to promote the expression of soluble taFv; however, whether these linker sequences are applicable to other taFv is unclear. Additionally, the peptide tag usually required for purification may affect the function of small BsAbs in samples prepared using bacterial or mammalian expression systems. We previously developed a method for the preparation of high quality, tag-free small BsAb using the Fc fusion format and protease digestion (17). Here, we applied this technique to prepare small BsAbs for comparative analyses (Fig. 1, *A* and *B*, and Fig. 6, *A* and *B*).

We previously reported that hEx3-Db functions comparably to its single-chain form, hEx3-scDb (23, 24). However, in the present study, the taFv format showed a more intense cytotoxicity than the Db format in both small and IgG-like BsAb constructs (Fig. 2). Comparisons of hEx3-Db, -scDb, and -taFv showed that the differences in their growth inhibition effects were correlated with structural differences in cross-linking between target cells (Fig. 3*A*) but not with differences in binding affinities (Tables 1 and 2). Interestingly, comparable cross-linking ability for soluble antigens was observed in all BsAbs in SPR imaging (Fig. 3*B*). These results suggest that diabodies with low flexibility may be susceptible to steric hindrance from other cell surface molecules in cross-linking between cells.

Multimerization of small recombinant antibodies, including BsAbs, is one available strategy for improving their pharmacokinetics and binding affinity (29–32). Recently, we also reported the highly enhanced activity of a dimeric hEx3-Db (hEx3 tetrabody) (22). Although the conformation is still unknown, the dimeric form was also found in prepared hEx3-taFv (Fig. 1*C*) and showed increased cytotoxicity (Fig. 5). Furthermore, to stabilize this noncovalent dimer, a disulfide-

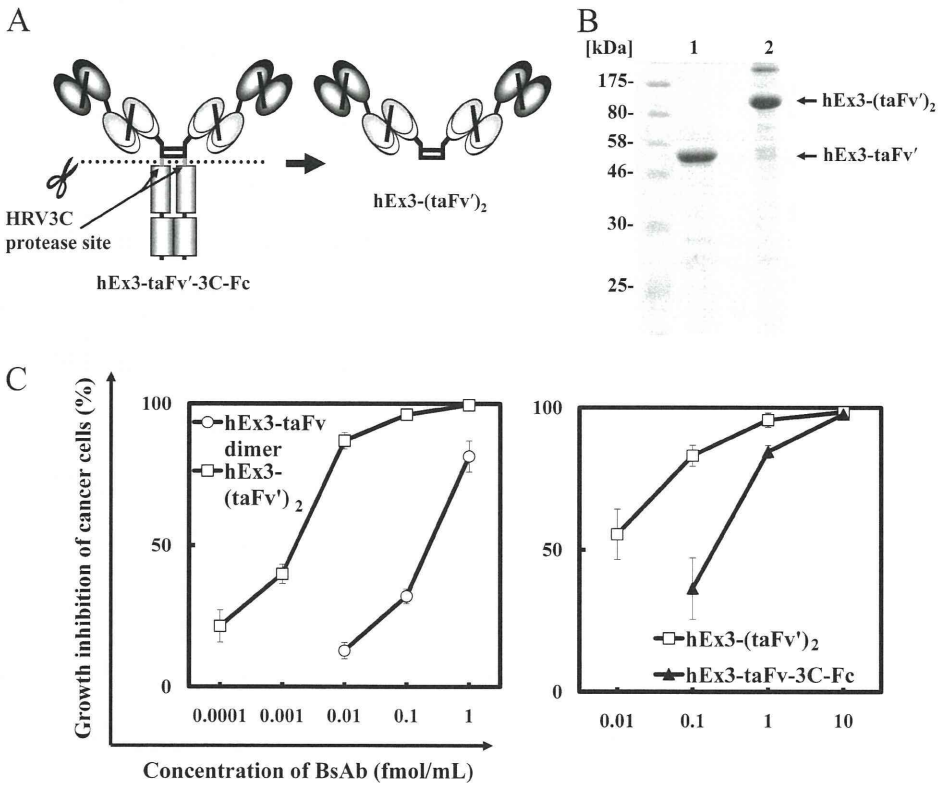

FIGURE 6. *A*, schematic illustration of the hEx3-taFv'-3C-Fc fusion protein. The HRV3C protease cleavage site used for preparation of hEx3-(taFv')$_2$ is indicated. *B*, SDS-PAGE of purified hEx3-(taFv')$_2$ under reducing conditions (*lane 1*) and nonreducing conditions (*lane 2*). *C*, growth inhibition of EGFR-positive TFK-1 cells by BsAbs. BsAbs and T-LAK cells were added to TFK-1 cells at a ratio of 5:1. Data are presented as the mean value ± S.D. and are representative of at least three independent experiments with similar results.

TABLE 2

K_A value for sEGFR and CD3$\epsilon\gamma$ evaluated by isothermal titration calorimetry

	K_A (sEGFR)	K_A (CD3$\epsilon\gamma$)
	$\times 10^7\ M^{-1}$	$\times 10^7\ M^{-1}$
hEx3-Db[a]	2.0	0.5
hEx3-scDb	1.8	13.8
hEx3-taFv	0.9	4.3

[a] Data from our previous report (22) are shown.

linked dimer was prepared by the Fc fusion method. The resulting hEx3-(taFv')$_2$ showed more-intense growth inhibition effects in comparison not only with the hEx3-taFv dimer but also with hEx3-taFv-3C-Fc (Fig. 6, *B* and *C*). Although *in vivo* experiments are now under way and may show different results due to additive Fc-mediated effector functions, the *in vitro* experiments show that the Fc region might cause steric hindrance in effective cross-linking.

To date, several studies have compared various small BsAb formats, including multimeric formats, and their differences in function; however, no consensus had been established on the most appropriate format (15, 33, 34). A previous comparative study of scDb and scFv formats (15), for example, showed that both have similar biological activities *in vitro*, and these results differ from our results. This difference between results may suggest that the most suitable format of small BsAbs depends on the Fv used and/or their combination, but it seems clear, at least, that converting formats has the potential to increase functionality. Furthermore, a previous report (35) and our unpublished data showed that the orientation of the variable domains of the Db can influence expression and formation of active binding sites. Thus, even when the same format is used, optimization of the local structure can also contribute to the improvement of function.

In conclusion, converting the format of small BsAbs can enhance their function. Particularly, a functional orientation that avoids steric hindrance in cross-linking between target cells can enhance the growth inhibition effect of small BsAbs targeting tumor and immune cells. Our results suggest that the taFv format may be suitable for hEx3 targeting EGFR and CD3. However, the yield of hEx3-taFv was lower than that of hEx3-Db prepared from the same procedure (22). To increase the productivity of hEx3-taFv for therapeutic application, we are working to use a variety of mammalian expression vectors and selection/amplification protocols (36).

REFERENCES

1. Cao, Y., and Lam, L. (2003) *Adv. Drug Deliv. Rev.* **55,** 171–197
2. Kufer, P., Lutterbüse, R., and Baeuerle, P. A. (2004) *Trends Biotechnol.* **22,** 238–244
3. Raso, V., and Griffin, T. (1981) *Cancer Res.* **41,** 2073–2078
4. Suresh, M. R., Cuello, A. C., and Milstein, C. (1986) *Methods Enzymol.* **121,** 210–228
5. Kriangkum, J., Xu, B., Nagata, L. P., Fulton, R. E., and Suresh, M. R. (2001) *Biomol. Eng.* **18,** 31–40
6. Holliger, P., and Winter, G. (1997) *Cancer Immunol. Immunother.* **45,** 128–130
7. Alt, M., Müller, R., and Kontermann, R. E. (1999) *FEBS Lett.* **454,** 90–94
8. Schlereth, B., Fichtner, I., Lorenczewski, G., Kleindienst, P., Brischwein,

K., da Silva, A., Kufer, P., Lutterbuese, R., Junghahn, I., Kasimir-Bauer, S., Wimberger, P., Kimmig, R., and Baeuerle, P. A. (2005) *Cancer Res.* **65,** 2882–2889
9. Shahied, L. S., Tang, Y., Alpaugh, R. K., Somer, R., Greenspon, D., and Weiner, L. M. (2004) *J. Biol. Chem.* **279,** 53907–53914
10. Robinson, M. K., Doss, M., Shaller, C., Narayanan, D., Marks, J. D., Adler, L. P., González Trotter, D. E., and Adams, G. P. (2005) *Cancer Res.* **65,** 1471–1478
11. Sundaresan, G., Yazaki, P. J., Shively, J. E., Finn, R. D., Larson, S. M., Raubitschek, A. A., Williams, L. E., Chatziioannou, A. F., Gambhir, S. S., and Wu, A. M. (2003) *J. Nucl. Med.* **44,** 1962–1969
12. Kipriyanov, S. M., Moldenhauer, G., Schuhmacher, J., Cochlovius, B., Von der Lieth, C. W., Matys, E. R., and Little, M. (1999) *J. Mol. Biol.* **293,** 41–56
13. Bühler, P., Wolf, P., Gierschner, D., Schaber, I., Katzenwadel, A., Schultze-Seemann, W., Wetterauer, U., Tacke, M., Swamy, M., Schamel, W. W., and Elsässer-Beile, U. (2008) *Cancer Immunol. Immunother.* **57,** 43–52
14. Kontermann, R. E. (2005) *Acta Pharmacol. Sin.* **26,** 1–9
15. Korn, T., Nettelbeck, D. M., Völkel, T., Müller, R., and Kontermann, R. E. (2004) *J. Gene Med.* **6,** 642–651
16. Asano, R., Sone, Y., Makabe, K., Tsumoto, K., Hayashi, H., Katayose, Y., Unno, M., Kudo, T., and Kumagai, I. (2006) *Clin. Cancer Res.* **12,** 4036–4042
17. Asano, R., Ikoma, K., Kawaguchi, H., Ishiyama, Y., Nakanishi, T., Umetsu, M., Hayashi, H., Katayose, Y., Unno, M., Kudo, T., and Kumagai, I. (2010) *FEBS J.* **277,** 477–487
18. Arakawa, F., Kuroki, M., Kuwahara, M., Senba, T., Ozaki, H., Matsuoka, Y., Misumi, Y., Kanda, H., and Watanabe, T. (1996) *J Biochem.* **120,** 657–662
19. Asano, R., Watanabe, Y., Kawaguchi, H., Fukazawa, H., Nakanishi, T., Umetsu, M., Hayashi, H., Katayose, Y., Unno, M., Kudo, T., and Kumagai, I. (2007) *J. Biol. Chem.* **282,** 27659–27665
20. Makabe, K., Nakanishi, T., Tsumoto, K., Tanaka, Y., Kondo, H., Umetsu, M., Sone, Y., Asano, R., and Kumagai, I. (2008) *J. Biol. Chem.* **283,** 1156–1166
21. Wiseman, T., Williston, S., Brandts, J. F., and Lin, L. N. (1989) *Anal. Biochem.* **179,** 131–137
22. Asano, R., Ikoma, K., Sone, Y., Kawaguchi, H., Taki, S., Hayashi, H., Nakanishi, T., Umetsu, M., Katayose, Y., Unno, M., Kudo, T., and Kumagai, I. (2010) *J. Biol. Chem.* **285,** 20844–20849
23. Asano, R., Kawaguchi, H., Watanabe, Y., Nakanishi, T., Umetsu, M., Hayashi, H., Katayose, Y., Unno, M., Kudo, T., and Kumagai, I. (2008) *J. Immunother.* **31,** 752–761
24. Asano, R., Sone, Y., Ikoma, K., Hayashi, H., Nakanishi, T., Umetsu, M., Katayose, Y., Unno, M., Kudo, T., and Kumagai, I. (2008) *Protein Eng. Des. Sel.* **21,** 597–603
25. De Jonge, J., Brissinck, J., Heirman, C., Demanet, C., Leo, O., Moser, M., and Thielemans, K. (1995) *Mol. Immunol.* **32,** 1405–1412
26. Mallender, W. D., and Voss, E. W., Jr. (1994) *J. Biol. Chem.* **269,** 199–206
27. Brandão, J. G., Scheper, R. J., Lougheed, S. M., Curiel, D. T., Tillman, B. W., Gerritsen, W. R., van den Eertwegh, A. J., Pinedo, H. M., Haisma, H. J., and de Gruijl, T. D. (2003) *Vaccine* **21,** 2268–2272
28. McCall, A. M., Adams, G. P., Amoroso, A. R., Nielsen, U. B., Zhang, L., Horak, E., Simmons, H., Schier, R., Marks, J. D., and Weiner, L. M. (1999) *Mol. Immunol.* **36,** 433–445
29. Pei, X. Y., Holliger, P., Murzin, A. G., and Williams, R. L. (1997) *Proc. Natl. Acad. Sci. U.S.A.* **94,** 9637–9642
30. Dolezal, O., Pearce, L. A., Lawrence, L. J., McCoy, A. J., Hudson, P. J., and Kortt, A. A. (2000) *Protein Eng.* **13,** 565–574
31. Power, B. E., Doughty, L., Shapira, D. R., Burns, J. E., Bayly, A. M., Caine, J. M., Liu, Z., Scott, A. M., Hudson, P. J., and Kortt, A. A. (2003) *Protein Sci.* **12,** 734–747
32. Le Gall, F., Reusch, U., Moldenhauer, G., Little, M., and Kipriyanov, S. M. (2004) *J. Immunol. Methods* **285,** 111–127
33. Kipriyanov, S. M., Moldenhauer, G., Braunagel, M., Reusch, U., Cochlovius, B., Le Gall, F., Kouprianova, O. A., Von der Lieth, C. W., and Little, M. (2003) *J. Mol. Biol.* **330,** 99–111
34. Mølhøj, M., Crommer, S., Brischwein, K., Rau, D., Sriskandarajah, M., Hoffmann, P., Kufer, P., Hofmeister, R., and Baeuerle, P. A. (2007) *Mol. Immunol.* **44,** 1935–1943
35. Lu, D., Jimenez, X., Witte, L., and Zhu, Z. (2004) *Biochem. Biophys. Res. Commun.* **318,** 507–513
36. Trill, J. J., Shatzman, A. R., and Ganguly, S. (1995) *Curr. Opin. Biotechnol.* **6,** 553–560

Journal of Bioscience and Bioengineering
VOL. 111 No. 2, 140–145, 2011

ELSEVIER

www.elsevier.com/locate/jbiosc

Material-binding peptide application—ZnO crystal structure control by means of a ZnO-binding peptide

Takanari Togashi,[1] Nozomi Yokoo,[2] Mitsuo Umetsu,[3,4,*] Satoshi Ohara,[5] Takashi Naka,[6] Seiichi Takami,[2] Hiroya Abe,[5] Izumi Kumagai,[3] and Tadafumi Adschiri[1]

Advanced Institute for Materials Research, WPI, Tohoku University, 2-1-1 Katahira, Aoba-ku, Sendai 980-8577, Japan,[1] Institute of Multidisciplinary Research for Advanced Materials, Tohoku University, 2-1-1 Katahira, Aoba-ku, Sendai 980-8577, Japan,[2] Department of Biomolecular Engineering, Graduate School of Engineering, Tohoku University, 6-6-11 Aoba, Aramaki, Aoba-ku, Sendai 980-8579, Japan,[3] Center for Interdisciplinary Research, Tohoku University, 6-3 Aoba, Aramaki, Aoba-ku, Sendai 980-8578, Japan,[4] Joining and Welding Research Institute, Osaka University, 11-1 Mihogaoka, Ibaraki, Osaka, 567-0047 Japan,[5] and Innovative Materials Engineering Laboratory, National Institute for Material Science, 1-2-1 Sengen, Tsukuba, Ibaraki 305-0047, Japan[6]

Received 3 July 2010; accepted 23 September 2010
Available online 13 October 2010

Recently, a zinc oxide (ZnO)-binding peptide (ZnOBP) has been identified and has been used to assist the synthesis of unique crystalline ZnO particles. We analyzed the influence of ZnOBP on the crystal growth of ZnO structures formed from zinc hydroxide. The addition of ZnOBP in the hydrothermal synthesis of ZnO suppressed [0001] crystal growth in the ZnO particles, indicating that the specificity of the material-binding peptide for specific inorganic crystal faces controlled the crystal growth. Furthermore, the dipeptides with a partial sequence of ZnO-binding "hot spot" in ZnOBP were used to synthesize ZnO particles, and we found that the presence of these dipeptides more strictly suppressed (0001) growth in ZnO crystals than did the complete ZnOBP sequence. These results demonstrate the applicability of dipeptides selected from material-binding peptides to control inorganic crystal growth.

[**Key words:** Crystal growth control; Dipeptide; Inorganic material synthesis; Material-binding peptide]

The morphology of inorganic materials synthesized in solution is controlled by crystal face growth, and the growth rate of the crystal faces depends on the crystal structure of these materials. The synthesis of metal, semiconductor, and metal oxide particles with controlled shapes is of fundamental and technological interest, because the synthesis of shape-controlled particles allows for tuning of the particles' shape-dependent physical properties; thus, the particles may be optimized for promising applications in optics, catalysis, biosensing, and data storage (1,2). To this end, organic-solution phase (3–5) and liquid–solid-solution phase synthetic transfer routes (6) have been demonstrated to be versatile pathways toward the development of such shape-controlled metal oxide particles, because these methods allow for control of crystal face growth. In all of these methods, organic surfactants play a key role in determining the growth and stability of inorganic particles.

In biology, combinatorial library approaches have allowed researchers to identify artificial peptides and antibodies with affinity for nonbiological inorganic materials (7–10). These material-binding peptides can be used to directly pattern biomolecules and nanoparticles on inorganic substrates (11–13), and some peptides can be used to synthesize nanometer-to-micrometer-sized inorganic particles in neutral aqueous solution at room temperature (14–17). Such wet-chemical techniques, applied under mild conditions, are attracting growing interest because they are potentially useful for the deposition of inorganic materials in or on heat-labile or pH-sensitive organic compounds. Moreover, some materials synthesized by using material-binding peptides have unique crystalline structures, suggesting that material-binding peptides could be used as an interesting method to synthesize anisotropic inorganic particles (14,15,17). However, because the binding and biomineralization mechanisms of material-binding peptides have not yet been elucidated, these substances cannot yet be utilized to control the morphology of synthesized materials. Rational elucidation of the behavior of material-binding peptides in inorganic synthesis would allow these peptides to be utilized in a broad range of biomimetic approaches toward hybrid material synthesis.

Recently, a zinc oxide (ZnO)-binding peptide (ZnOBP) was identified, and the functionalization of ZnOBP via fusion with a cysteine-containing short peptide resulted in the formation of nanometer-sized ZnO crystallines, which were assembled to unique flower-like structures (17). In this study, we analyzed the influence of ZnOBP on the crystal growth of ZnO structures synthesized from zinc hydroxide ($Zn(OH)_2$) and observed the suppression of crystal growth

Abbreviations: SEM, scanning electron microscopy; XRD, X-ray diffraction; ZnO, zinc oxide; ZnOBP, zinc oxide-binding peptide.

* Corresponding author. Department of Biomolecular Engineering, Graduate School of Engineering, Tohoku University, 6-6-11 Aoba, Aramaki, Aoba-ku, Sendai 980-8579, Japan. Tel./fax: +81 22 795 7276.
E-mail address: mitsuo@kuma.che.tohoku.ac.jp (M. Umetsu).

1389-1723/$ - see front matter © 2010, The Society for Biotechnology, Japan. All rights reserved.
doi:10.1016/j.jbiosc.2010.09.013

in the [0001] direction by the addition of ZnOBP in the hydrothermal synthesis of ZnO. The binding properties of ZnOBP have been physicochemically analyzed previously, and a "hot spot" peptide sequence for ZnO binding has been identified (18). A dipeptide with the same sequence as that of the ZnOBP hot spot was also used to synthesize ZnO particles from $Zn(OH)_2$, and critical suppression of ZnO crystal growth was observed. We describe the potential of dipeptide molecules for controlling the morphology control of synthesized materials.

MATERIALS AND METHODS

An organically synthesized peptide with the ZnOBP sequence (EAHVMHKVAPRP), where the amine and carboxyl groups of the main chain at the N- and C-terminus are inactivated by acetylation and amidation, respectively, was purchased from Peptide Institute, Inc. (Osaka, Japan). The amino acids and the dipeptides also were purchased from Peptide Institute, Inc.

For the ZnOBP-assisted synthesis of ZnO particles, a 0.1 M zinc nitrate solution was mixed with the same volume of 0.2 M potassium hydrate to produce $Zn(OH)_2$. The produced $Zn(OH)_2$ was rinsed several times with distilled water, and the final concentration of $Zn(OH)_2$ was adjusted to 0.1 M. After 1 mg of ZnOBP (690 nmol) were added to 1 ml of the $Zn(OH)_2$ solution, the solution was heated in a closed vessel at 95°C for 24 h to synthesize ZnO. The heated solid material was centrifuged, and the precipitates were rinsed several times with distilled water and then dried in vacuo, yielding ZnO particles. The supernatant was analyzed on a size-exclusion chromatography column (Asahipak GS-220 HQ, Shodex, Tokyo, Japan) equilibrated with H_2O. As an alternative ZnO synthesis, the $Zn(OH)_2$ solution was dried at 95°C in an open vessel for 24 h. For the application of amino acids or dipeptide instead of ZnOBP, we added 690 nmol of them in the $Zn(OH)_2$ solution.

For analyzing the structure of synthesized materials, scanning electron microscopy (SEM) images were obtained on a Philips XL30 ESEM instrument operating at 15 keV. Samples were dried in a vacuum and coated with platinum by means of an ion-coating instrument. X-ray diffraction (XRD) patterns were also recorded with a RINT-2000 spectrometer (Rigaku, Tokyo, Japan) with Cu Kα radiation. Samples were dried in a vacuum before XRD experiments.

RESULTS AND DISCUSSION

To analyze the influence of the material-binding peptide on ZnO synthesis, ZnOBP molecules were added to a $Zn(OH)_2$ solution, and the solution was boiled at 95°C for 24 h to synthesize ZnO particles. Without ZnOBP, needle-type ZnO structures were synthesized (Fig. 1a), whereas addition of ZnOBP resulted in the formation of ZnO needles with flattened edges (Fig. 1b). This structural change induced by the addition of ZnOBP was also observed for ZnO synthesized by means of drying rather than boiling. Changing the dehydration process from boiling to drying caused no structural changes in the ZnO particles synthesized without peptides (data not shown); however, the $Zn(OH)_2$ solution containing ZnOBP formed ZnO particles with peanut-like structures when the drying method was used (Fig. 1c). These structural changes imply that the addition of ZnOBP influenced [0001] crystal growth in the resulting ZnO particles. In the drying method, peptide, ZnO ion, and produced ZnO particles are being concentrated in the process of ZnO synthesis. We consider that the gradual concentration change causes the formation of peanut-like structure.

Fig. 2 shows the XRD pattern of synthesized ZnO materials. The needle-type ZnO structures synthesized without ZnOBP exhibited strong diffraction derived from (100) crystal faces (Fig. 2a), whereas the diffraction was relatively weak in the XRD patterns of ZnO particles synthesized by boiling or by drying with ZnOBP (Fig. 2b and c). These results suggest that the presence of ZnOBP during ZnO synthesis suppressed ZnO crystal growth in the [0001] direction, in agreement with the SEM images shown in Fig. 1. Comparison of the XRD patterns of the ZnO particles synthesized by boiling with those obtained by drying with ZnOBP, in the presence of ZnOBP, revealed that the peanut-like ZnO structures obtained by drying had a weaker (100) diffraction than did the ZnO structures obtained by boiling. This difference in diffraction patterns might indicate that the peanut-like structures had more suppressed [0001] crystal orientation, or that they had more (101) crystal faces, than did the ZnO structure obtained by boiling.

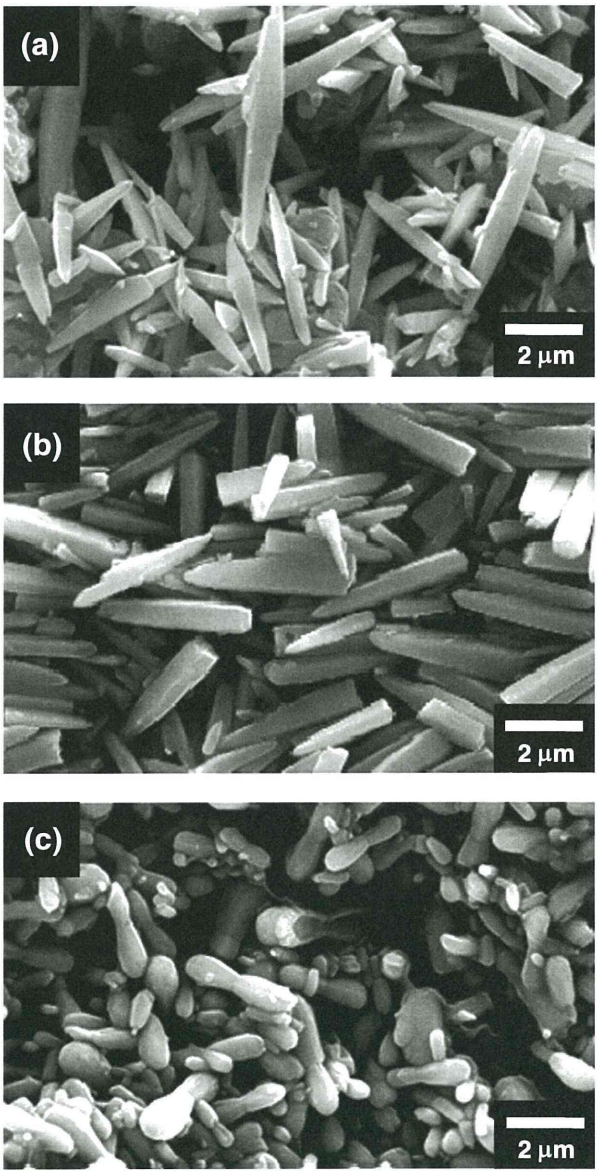

FIG. 1. SEM images of ZnO particles synthesized by boiling 0.1 M $Zn(OH)_2$ solution at 95°C (a) without ZnOBP and (b) with 690 nmol of ZnOBP and of (c) ZnO particles synthesized by drying 0.1 M $Zn(OH)_2$ at 95°C with 690 nmol of ZnOBP.

In our previous report, we identified the sequence around sixth histidine residue in ZnOBP as the hot spot for binding to the ZnO surface (18). Here, we analyzed the influence of the dipeptides with sixth histidine residue, Met-His (fifth–sixth) and His-Lys (sixth–seventh), on ZnO synthesis. When we added the dipeptide Ala-Ala to the ZnO solution as a control peptide and boiled the solution to synthesize ZnO, we observed the same needle-type ZnO particles that were observed for ZnO synthesized without any peptides (Fig. 3a). In contrast, the addition of the dipeptide Met-His resulted in the synthesis of stick-type particles with flatter edges than those of the ZnO rod particles synthesized with intact ZnOBP (Fig. 3b). Moreover, such flattening of synthesized ZnO particle edges was also observed when the dipeptide His-Lys was added to the ZnO solution (Fig. 3c). This flattening of ZnO edges was not observed when mixtures of amino acid monomers (Met and His, His and Lys) were added in the

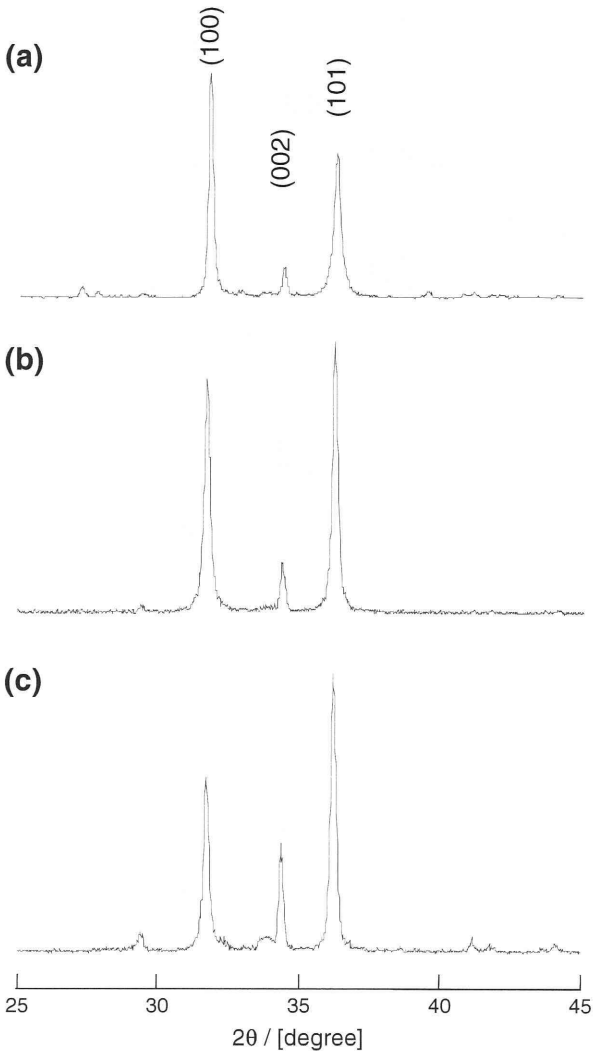

FIG. 2. XRD patterns of ZnO particles synthesized by boiling 0.1 M $Zn(OH)_2$ solution at 95°C (a) without ZnOBP and (b) with 690 nmol of ZnOBP and of (c) ZnO particles synthesized by drying 0.1 M $Zn(OH)_2$ at 95°C with 690 nmol of ZnOBP.

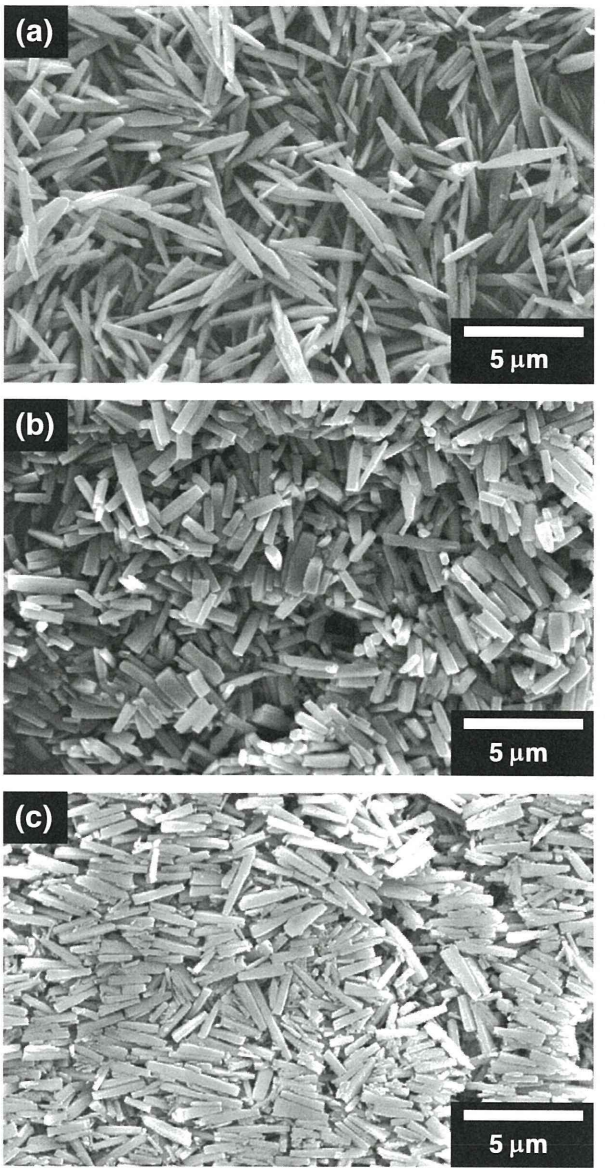

FIG. 3. SEM images of ZnO particles synthesized by boiling 0.1 M $Zn(OH)_2$ solution at 95°C with the dipeptide of (a) Ala-Ala, (b) Met-His, and (c) His-Lys. For all syntheses, the amount of the added dipeptides was 690 nmol.

ZnO synthesis; however, needle-type ZnO particles were formed in those cases (data not shown). In addition, we also analyzed the influence of the dipeptides with third histidine residue, Ala–His (second–third) and His–Val (third–fourth), on ZnO synthesis; however, the presence of the dipeptides did not cause the flattening of ZnO edge (data not shown). Hence, the formation of flattened ZnO edges upon the addition of the Met–His (fifth–sixth) and His–Lys (sixth–seventh) dipeptides indicates that the hot spot sequence in ZnOBP was preferentially bound to the edge area of the ZnO particles in the ZnO synthesis process; it also suggests that the removal of other sequences except for the hot spot residue promotes suppression of [0001] crystal growth in the ZnO synthesis process by capping effect.

To observe the dipeptides' ability to control the structure of synthesized ZnO particles, we synthesized ZnO particles from $Zn(OH)_2$ by boiling the solution with different concentrations of His–Lys dipeptides (Fig. 4). As the amount of added dipeptides increased, the edges of the synthesized ZnO rod particles were flattened at the dipeptide concentration of 690 nmol and the length of the particles decreased. Therefore, the increase in added dipeptides apparently promoted a capping effect for ZnO growth, suppressing the longitudinal growth of ZnO so that the synthesized particles were anisotropically downsized.

ZnO is one of the most widely studied metal oxides for use in solar cells (19), sensors (20), ultraviolet nanolasers (21), and blue-light-emitting diodes (22), because ZnO is a semiconductor with a wide direct band gap that possesses unique optical, acoustic, and electronic properties. This wide variety of applications requires the fabrication of morphologically and functionally distinct ZnO nanostructures; consequently, a large number of studies of morphology control of ZnO have been reported (23–26). In the wet-chemical approaches, kinetic energy barriers, temperature, time, and capping molecules are considered to be factors that can influence the crystal growth of synthesized inorganic materials (27). Among these parameters, capping molecules play two important roles: the creation of appropriate environments where crystal growth is promoted (23) and the selective adsorption of the capping molecules onto specific crystal faces to control the growth rate of capped surfaces (25,28). In

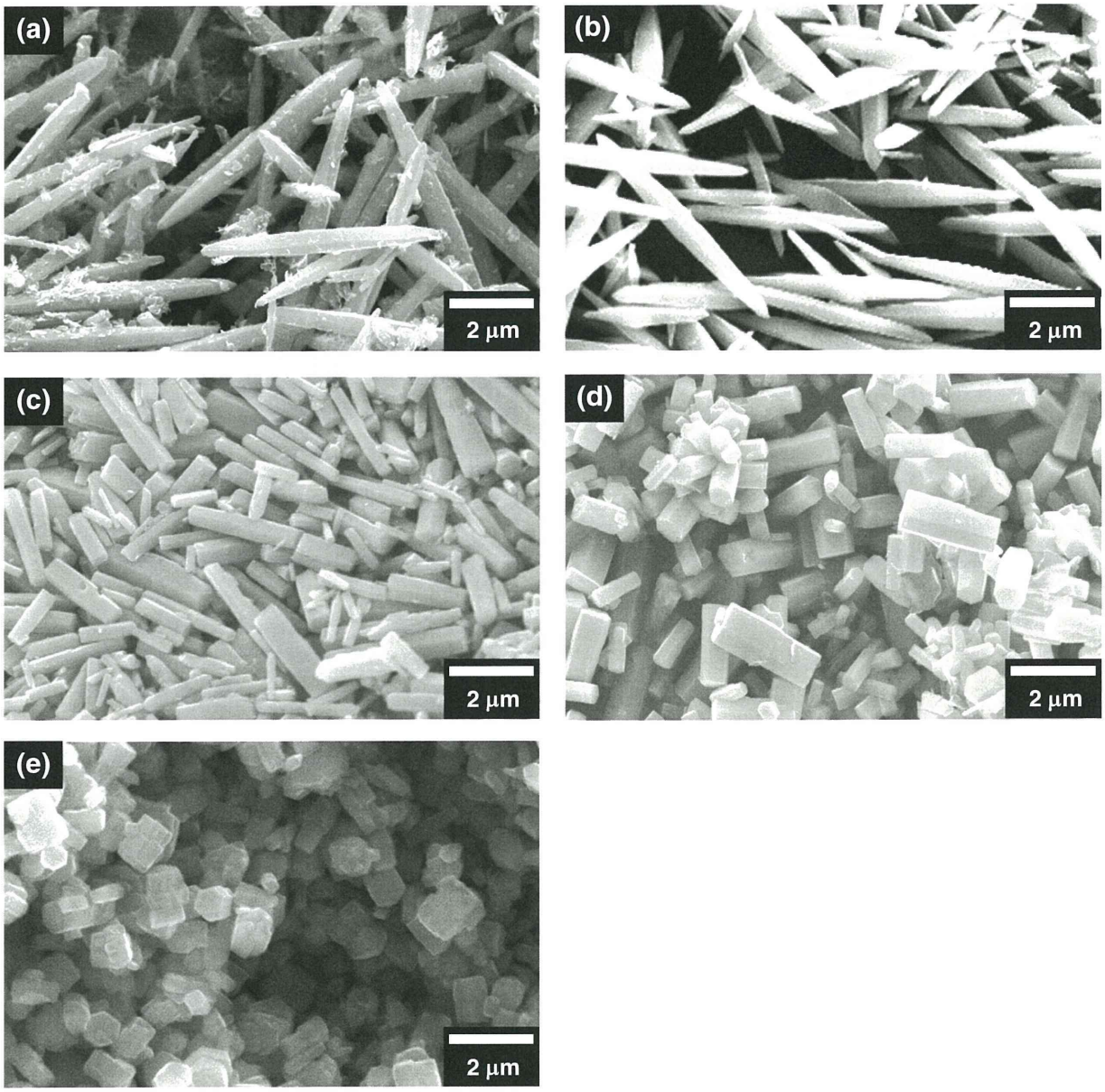

FIG. 4. SEM images of ZnO particles synthesized by boiling $Zn(OH)_2$ solution at 95°C with (a) 0 nmol, (b) 345 nmol, (c) 690 nmol, and (d) 1380 nmol, and (e) 2760 nmol of the dipeptide His-Lys.

this study, we demonstrated the suppression of [0001] crystal growth in ZnO particles in the presence of ZnOBP, particularly in the presence of dipeptides of Met–His and His–Lys, which have been identified as partial sequences of the ZnO-binding hot spot sequence in ZnOBP. Our results suggest preferential adsorption of the hot spot sequence in ZnOBP onto the (0001) crystal faces of ZnO hexagonal structures. For analyzing the stability of ZnOBP at 95 °C in water, we analyzed the peptide solution heated for 24 h, using liquid chromatography (Fig. 5); consequently, few ZnOBPs were hydrolyzed. This result suggests that other peptide sequence in ZnOBP interfere the preferentially binding of Met–His and His–Lys dipeptides onto (0001) crystal faces.

Recently, Tomczak et al. synthesized ZnO from zinc nitrate hexahydrate ($Zn(NO_3)_2$) by using amine molecules at low temperature (29). The addition of another ZnO-binding peptide called Z1 peptide (GLHVMHKVAPPA) inhibited the [0001] crystal growth in the ZnO particles. It should be noted that the sequence HVMHKVAP in the Z1 peptide is identical to the sequence in the hot spot region of ZnOBP. Therefore, the Met–His and His–Lys sequences in HVMHKVAP appear to have a capping effect for ZnO synthesized from both ($Zn(NO_3)_2$) and $Zn(OH)_2$ precursors.

Met, His, and Lys composed of the dipeptide inhibiting the [0001] crystal growth in the ZnO particles (His–Lys and Met–His) have a functional group that can coordinate metal atoms: proteins with metal atoms that are coordinated by these amino acids have been reported (30,31). (1010) and (1120) crystal surfaces of ZnO are formed by the same number of Zn and O, while only one species of atom (Zn or O) appears on (0001) surface (32–34). Although we have no direct evidence, we consider that the dipeptide should prefer the binding onto the Zn-terminated (0001) surface of ZnO. In our study, ZnO morphology could not be controlled by a His amino acid and the dipeptides with His and non-polar amino acids (His–Ala and His–Val:

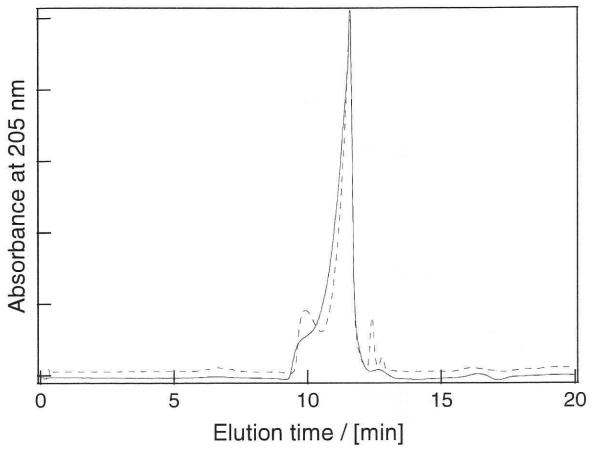

FIG. 5. Size-exclusion chromatography of ZnOBP before boiling at 95 °C for 24 h (solid line) and after boiling at 95 °C for 24 h (dotted line). A 50 μl of 1 mg/ml sample was applied at the flow rate of 0.5 ml/min to a column of Asahipak GS-220 HQ; the absorbance of the eluent was monitored at 205 nm.

second–third and third–fourth sequence of ZnOBP, respectively). These results support our consideration that the presence of two metal-affinitive amino acids in dipeptide results in preference interaction with (0001) crystal face of ZnO.

In our previous report, we synthesized ZnO crystals from $Zn(OH)_2$ at room temperature by using ZnOBP with a GGGSC sequence fused to the binding peptide's C-terminus (17). The addition of GGGSC-fused ZnOBP to $Zn(OH)_2$ required no heat treatment to synthesize ZnO nanoparticles with the size of 10 nm and the synthesized nanoparticles spontaneously assembled to flower-like aggregates. Although the formation mechanism of this flower-like aggregates has not been elucidated yet, the capping effect of ZnOBP at low temperature might have extremely retarded the growth rate of the ZnO crystals, causing the 10-nm nanoparticles to form.

In conclusion, the ZnO-binding peptide ZnOBP, which was composed of the sequence EAHVMHKVAPRP, suppressed [0001] crystal growth in the ZnO particles. Dipeptides containing amino acids found in the identified ZnO-binding hot spot region in ZnOBP promoted the suppression of (0001) growth in ZnO crystals more so than did the complete ZnOBP sequence. Hence, the material-binding peptide's recognition of specific inorganic crystal faces was utilized to control the direction of crystal growth. Peptides with a more specific recognition of crystal faces would afford even greater control of crystal morphology than that demonstrated here. The selection with highly-specific peptides against ZnO crystal face is in progress.

ACKNOWLEDGMENTS

This work was supported by a Scientific Research Grant from the Ministry of Education, Science, Sports, and Culture of Japan (M.U.), by the Industrial Technology Research Grant Program 2005 of the New Energy and Industrial Technology Development Organization (NEDO) of Japan (M.U.), and by Precursory Research for Embryonic Science and Technology from the Japan Science and Technology Agency (JST). This research was also partly supported by the Association for the Progress of New Chemistry foundation (M.U.).

References

1. **Peng, X.:** Mechanisms for the shape-control and shape-evolution of colloidal semiconductor nanocrystals, Adv. Mater., **15**, 459–463 (2003).
2. **Burda, C., Chen, X., Narayanan, R., and El-Sayed, M. A.:** Chemistry and property of nanocrystals of different shapes, Chem. Rev., **105**, 1025–1102 (2005).
3. **Hyeon, T., Lee, S. S., Park, J., Chung, Y., and Na, H. B.:** Synthesis of highly crystalline and monodisperse maghemite nanocrystallites without a size-selection process, J. Am. Chem. Soc., **123**, 12798–12801 (2001).
4. **Rockenberger, J., Scher, E. C., and Alivisatos, A. P.:** A New Nonhydrolytic Single-Precursor Approach to Surfactant-Capped Nanocrystals of Transition Metal Oxides, J. Am. Chem. Soc., **121**, 11595–11596 (1996).
5. **Park, J., An, K., Hwang, Y., Park, J.-G., Noh, H.-J., Kim, J.-Y., Park, J.-H., Hwang, N.-M., and Hyeon, T.:** Ultra-large-scale syntheses of monodisperse nanocrystals, Nat. Mater., **3**, 891–895 (2004).
6. **Wang, X., Zhuang, J., Peng, Q., and Li, Y.:** A general strategy for nanocrystal synthesis, Nature, **437**, 121–124 (2005).
7. **Whaley, S. R., English, D. S., Hu, E. L., Barbara, P. F., and Belcher, A. M.:** Selection of peptides with semiconductor binding specificity for directed nanocrystal assembly, Nature, **405**, 665–668 (2000).
8. **Sarikaya, M., Tamerler, C., Jen, A. K.-Y., Schulten, K., and Baneyx, F.:** Molecular biomimetics: nanotechnology through biology, Nat. Mater., **2**, 577–585 (2003).
9. **Watanabe, H., Nakanishi, T., Umetsu, M., and Kumagai, I.:** Human anti-gold antibodies: biofunctionalization of gold nanoparticles and surfaces with anti-gold antibodies, J. Biol. Chem., **283**, 36031–36038 (2008).
10. **Hattori, T., Umetsu, M., Nakanishi, T., Togashi, T., Yokoo, N., Abe, H., Ohara, S., Adschiri, T., and Kumagai, I.:** High affinity anti-inorganic material antibody generation by integrating graft and evolution technologies. Potential of antibodies as biointerface molecules, J. Biol. Chem., **285**, 7784–7793 (2010).
11. **Park, T. J., Lee, S. Y., Lee, S. J., Park, J. P., Yang, K. S., Lee, K.-B., Ko, S., Park, J. B., Kim, T., Kim, S. K., and other 5 authors:** Protein nanopatterns and biosensors using gold binding polypeptide as a fusion partner, Anal. Chem., **78**, 7197–7205 (2006).
12. **Kacar, T., Ray, J., Gungormus, M., Oren, E. E., Tamerler, C., and Sarikaya, M.:** Quartz binding peptides as molecular linkers towards fabricating multifunctional micropatterned substrates, Adv. Mater., **21**, 295–299 (2009).
13. **Umetsu, M., Hattori, T., Kikuchi, S., Muto, I., Nakanishi, T., Watanabe, H., and Kumagai, I.:** Nanoparticles with affinity for biopolymer: bioassisted room-temperature selective multistacking of inorganic particles on biopolymer film, J. Mater. Res., **23**, 3241–3246 (2008).
14. **Brown, S., Sarikaya, M., and Johnson, E. A.:** Genetic Analysis of Crystal Growth, J. Mol. Biol., **299**, 725–735 (2000).
15. **Naik, R. R., Stringer, S. J., Agarwal, G., Jones, S. E., and Stone, M. O.:** Biomimetic synthesis and patterning of silver nanoparticles, Nat. Mater., **1**, 169–172 (2002).
16. **Mao, C., Flynn, C. E., Hayhurst, A., Sweeney, R., Qi, J., Georgiou, G., Iverson, B., and Belcher, A. M.:** Viral assembly of oriented quantum dot nanowires, Proc. Natl. Acad. Sci. U. S. A., **100**, 6946–6951 (2003).
17. **Umetsu, M., Mizuta, M., Tsumoto, K., Ohara, S., Takami, S., Watanabe, H., Kumagai, I., and Adschiri, T.:** Bioassisted room-temperature immobilization and mineralization of zinc oxide—the structural ordering of zno nanoparticles into a flower-type morphology, Adv. Mater., **17**, 2571–2575 (2005).
18. **Yokoo, N., Togashi, T., Umetsu, M., Tsumoto, K., Hattori, T., Nakanishi, T., Ohara, S., Takami, S., Naka, T., Abe, H., Kumagai, I., and Adschiri, T.:** Direct and selective immobilization of proteins by means of an inorganic material-binding peptide: discussion on functionalization in the elongation to material-binding peptide, J. Phys. Chem. B, **114**, 480–486 (2010).
19. **O'Regan, B., Schwartz, D. T., Zakeeruddin, S. M., and Grätzel, M.:** Electrodeposited nanocomposite n–p heterojunctions for solid-state dye-sensitized photovoltaics, Adv. Mater., **12**, 1263–1267 (2000).
20. **Lin, H.-M., Tzeng, S.-J., Hsiau, P.-J., and Tsai, W.-L.:** Electrode effects on gas sensing properties of nanocrystalline zinc oxide, Nanostruct. Mater., **10**, 465–477 (1998).
21. **Huang, M. H., Mao, S., Feick, H., Yan, H., Wu, Y., Kind, H., Weber, E., Russo, R., and Yang, P.:** Room-temperature ultraviolet nanowire nanolasers, Science, **292**, 1897–1899 (2001).
22. **Tsukazaki, A., Ohtomo, A., Onuma, T., Ohtani, M., Makino, T., Sumiya, M., Ohtani, K., Chichibu, S. F., Fuke, S., Segawa, Y., and other 3 authors:** Repeated temperature modulation epitaxy for p-type doping and light-emitting diode based on ZnO, Nat. Mater., **4**, 42–46 (2005).
23. **Zhang, H., Yang, D., Ji, Y., Ma, X., Xu, J., and Que, D.:** Low temperature synthesis of flowerlike ZnO nanostructures by cetyltrimethylammonium bromide-assisted hydrothermal process, J. Phys. Chem. B, **108**, 3955–3958 (2004).
24. **Pan, Z. W., Dai, Z. R., and Wang, Z. L.:** Nanobelts of semiconducting oxides, Science, **291**, 1947–1949 (2001).
25. **Tain, Z. R., Voigt, J. A., Liu, J., Mckenzie, B., and Mcdermott, M. J.:** Biomimetic arrays of oriented helical Zno nanorods and columns, J. Am. Chem. Soc., **124**, 12954–12955 (2002).
26. **Tain, Z. R., Voigt, J. A., Liu, J., Mckenzie, B., Mcdermott, M. J., Rodriguez, M. A., Konishi, H., and Xu, H.:** Complex and oriented ZnO nanostructures, Nat. Mater., **2**, 821–826 (2003).
27. **Lee, S. M., Cho, S. N., and Cheon, J. W.:** Anisotropic shape control of colloidal inorganic nanocrystals, Adv. Mater., **15**, 441–444 (2003).
28. **Gao, P., Ying, C., Wang, S., Ye, L., Guo, Q., and Xie, Y.:** Low temperature hydrothermal synthesis of ZnO nanodisk arrays utilizing self-assembly of surfactant molecules at solid-liquid interfaces, J. Nanopart. Res., **8**, 131–136 (2006).
29. **Tomczak, M. M., Gupta, M. K., Drummy, L. F., Rozenzhak, S. M., and Naik, R. R.:** Morphological control and assembly of zinc oxide using a biotemplate, Acta Biomater., **5**, 876–882 (2009).

30. **Shibata, N., Inoue, T., Nagano, C., Nishio, N., Kohzuma, T., Onodera, K., Yoshizaki, F., Sugimura, Y., and Kai, Y.:** Novel insight into the copper-ligand geometry in the crystal structure of *Ulva pertusa* plastocyanin at 1.6 Å resolution: structural basis for regulation of the copper site by residue 88, J. Biol. Chem., **274**, 4225–4230 (1999).
31. **Kawakami, N., Toshishige, M., Matsuo, M., Gekko, K., and Michibata, H.:** Characterization of vanadium-binding sites of the vanadium-binding protein Vanabin2 by site-directed mutagenesis, Biochim. Biophys. Acta, **1790**, 1327–1333 (2009).
32. **Özgür, Ü., Alivov, Y. I., Liu, C., Teke, A., Reshchikov, M. A., Doğan, S., Avrutin, V., Cho, S.-J., and Morkoç, H.:** A comprehensive review of ZnO materials and devices, J. Appl. Phys., **98**, 041301-1-109 (2005).
33. **Dulub, O., Boatner, L. A., and Diebold, U.:** STM study of the geometric and electronic structure of ZnO(0001)-Zn, (000–1)-O, (10–10), and (11–20) surfaces, Surf. Sci., **519**, 201–217 (2002).
34. **Noguera, C.:** Polar oxide surfaces, J. Phys. Condens. Matter, **12**, R367–R410 (2000).

ADVANCED FUNCTIONAL MATERIALS
www.afm-journal.de

Materials Views
www.MaterialsViews.com

Calcination- and Etching-Free Photolithography of Inorganic Phosphor Films Consisting of Rare Earth Ion Doped Nanoparticles on Plastic Sheets

Satoshi Watanabe, Hiroshi Hyodo, Hirohisa Taguchi, Kohei Soga, Yoshifumi Takanashi, and Mutsuyoshi Matsumoto*

It is demonstrated that patterned inorganic phosphor films consisting of rare earth ion doped nanoparticles (RE-NPs) can be fabricated on plastic sheets using calcination- and etching-free photolithography. Green up-conversion luminescence and near-infrared (NIR) fluorescence appears from the RE-NPs that are prepared from Y_2O_3 doped with 1 mol% Er^{3+} and 0.85 mol% Yb^{3+}. The diameter of the RE-NPs is estimated to be about 300 nm using dynamic light scattering. Visible transmittance of the RE-NP film fabricated by dip-coating is more than 90%. Patterned RE-NP films are obtained by dip-coating the RE-NPs on patterned photoresist films fabricated by UV exposure through a photomask, followed by selective removal of the photoresist. Optical, fluorescence, scanning electron, atomic force, and Kelvin probe force microscopies are used for the characterization of the patterned RE-NP films. The present methodology enables fabrication of patterned RE-NP films, not only on inorganic substrates but also on plastic sheets, with low cost and material consumption.

1. Introduction

Two-dimensional nanofabrication using top-down and bottom-up techniques has attracted much attention in recent years in various fields such as information, material, device, bio-, and environmental technologies. Top-down techniques that are used include photolithography,[1] electron-beam lithography,[2] soft lithography,[3] dip-pen lithography,[4] and near-field optical lithography.[5] Bottom-up techniques utilize such phenomena as microphase separation in block copolymer films and in binary polymer/solute mixtures,[6] two-dimensional phase separation in mixed Langmuir–Blodgett films,[7] and formation of nanolattices in phospholipid monolayers.[8]

Dr. S. Watanabe, Dr. H. Hyodo, Prof. K. Soga, Prof. Y. Takanashi, Prof. M. Matsumoto
Department of Materials Science and Technology
Tokyo University of Science
Yamazaki 2641, Noda 278-8510, Japan
E-mail: watasato@rs.noda.tus.ac.jp
Prof. H. Taguchi
Department of Information System Technology
Chukyo University
Kaizu-cho Tokodachi 101, Toyota, 470-0392, Japan

DOI: 10.1002/adfm.201100718

Inorganic phosphor films containing rare earth ions are expected to be applied to display, sensor, and emission materials because of their unique physical and chemical properties. Low-phonon inorganic materials containing rare earth ions exhibit up-conversion, where the rare earth ions emit visible light under stepwise infrared excitation.[9] Near-infrared (NIR) light can transmit through biological samples with low biodamage and is thus promising for use in bioimaging[10] and biosensing.[11] Two-photon excitation has been used for nanofabrication[12] and high-resolution observation.[13] The wavelength of the emitted light from the fluorescent nanoparticles can be tuned by adjusting the species and the concentrations of the doped rare-earth ions.[14]

Conventional photolithography involving etching processes enables us to obtain patterned inorganic phosphor films using electrophoretic deposition,[15] screen printing,[16] a sol-gel method,[17] and a polyvinyl alcohol slurry method.[18] Recently, capillary lithography[19] and soft lithography,[20] using both sol-gel and microcontact printing methods, have been applied to the fabrication of patterned inorganic phosphor films. These soft lithographic techniques are useful for the fabrication of patterned inorganic phosphor films without etching processes and with low material consumption. However, these soft lithographic techniques require the calcination of precursors of the inorganic phosphor films after patterning them onto solid substrates. New photolithographic techniques free from calcination and etching processes will be indispensable for the fabrication of patterned inorganic phosphor films as functional materials have been deposited on flexible substrates in many fields.[21]

In this study, we demonstrate the fabrication of patterned inorganic phosphor films consisting of rare earth ion doped nanoparticles (RE-NPs) on plastic sheets using calcination- and etching-free photolithography. RE-NPs are prepared by calcining the precursors. This feature allows the application of calcination-free processes to the fabrication of patterned inorganic phosphor films and enables us to fabricate inorganic phosphor films on flexible substrates such as polyethylene terephthalate (PET) and polydimethylsiloxane (PDMS). We employ an etching-free process with low cost and material consumption for the fabrication of

patterned phosphor films consisting of RE-NPs. The RE-NP films are characterized using optical, fluorescence, scanning electron, atomic force, and Kelvin probe force microscopies.

2. Results and Discussion

2.1. Optical and Adsorption Properties of RE-NPs

We investigated emission properties of the RE-NPs prepared for the fabrication of inorganic phosphor films.

Figure 1a shows a fluorescence spectrum of the RE-NPs. Green up-conversion luminescence at about 525 and 560 nm is attributed to the $^2H_{11/2}$–$^4I_{15/2}$ and $^4S_{3/2}$–$^4I_{15/2}$ transitions of Er^{3+}, respectively. Red up-conversion luminescence at about 660 nm is assigned to the $^4F_{9/2}$–$^4I_{15/2}$ transition. With variations in the concentrations of the doped Er^{3+} and Yb^{3+} ions, the relative intensity of the emission of green up-conversion luminescence to that of red up-conversion luminescence changes. Figure 1b shows an NIR fluorescence spectrum of the RE-NPs. NIR fluorescence at 1075 and 1550 nm is attributed to the $^2F_{5/2}$–$^2F_{7/2}$ and $^4I_{13/2}$–$^4I_{15/2}$ transitions of Yb^{3+} and Er^{3+}, respectively. The relative intensity of the emission at 1500 nm is larger than that of the 1075-nm peak, due to energy transfer from excited Yb^{3+} to Er^{3+}. Up-conversion luminescence is explained by considering the mechanism involving energy-transfer up-conversion, excited-state absorption, and photon avalanche,[22] which is characterized by multiple energy transfers between the sensitizer Yb^{3+} and the activator Er^{3+}. Figure 1c shows the energy-level diagram involved in this mechanism. Absorption of a NIR photon by Yb^{3+} and subsequent energy transfer from the excited $^2F_{5/2}$ level of Yb^{3+} to Er^{3+} promote Er^{3+} to the quasiresonant metastable $^4I_{11/2}$ level. Absorption of a second NIR photon by Yb^{3+} and subsequent energy transfer from this excited $^2F_{5/2}$ level of Yb^{3+} to the previously excited $^4I_{11/2}$ level of Er^{3+} promote Er^{3+} to the $^4F_{7/2}$ level. The two main emission lines centered at 525 and 560 nm correspond to the radiative $^2H_{11/2}$–$^4I_{15/2}$ and $^4S_{3/2}$–$^4I_{15/2}$ transitions of Er^{3+}, respectively. The red emission peaking at 660 nm arises from the $^4F_{9/2}$–$^4I_{15/2}$ transition. These results indicate that the RE-NPs serve as green and NIR fluorescent nanoparticles.

The transmittance of inorganic phosphor films should be high for use in displays and emitting devices. We investigated the transmittance of the RE-NP films in the visible region. We also investigated the stability of the RE-NP films during immersion in acetone, which is used in the lift-off processes for photolithography.

Figure 2a shows a visible transmission spectrum of the RE-NP film dip-coated onto a glass plate. The transmittance of the RE-NP film is more than 90% in the visible region, and is comparable to that of inorganic phosphor films fabricated by the combination of a sol-gel method and soft lithography.[19,20] Transmittance in the shorter wavelength region decreases due to Rayleigh scattering. Figure 2b shows relative transmittance of the RE-NP film at 440 nm as a function of immersion time. The relative transmittance means the transmittance of the RE-NP film normalized to that of the as-fabricated RE-NP film. The relative transmittance of the RE-NP film remains unchanged during the immersion in acetone at room temperature. The immersion of the RE-NP films in water or hexane gave similar results. Subsequent ultrasonication in acetone drastically decreases the relative transmittance of the RE-NP film, which is caused by the desorption of RE-NPs from the RE-NP film, and indicates that the RE-NPs are physically adsorbed onto the glass plate. These results indicate that the RE-NP films have high transmittance in the visible region. In addition, the RE-NP films are stable to immersion in acetone, hexane, and water at

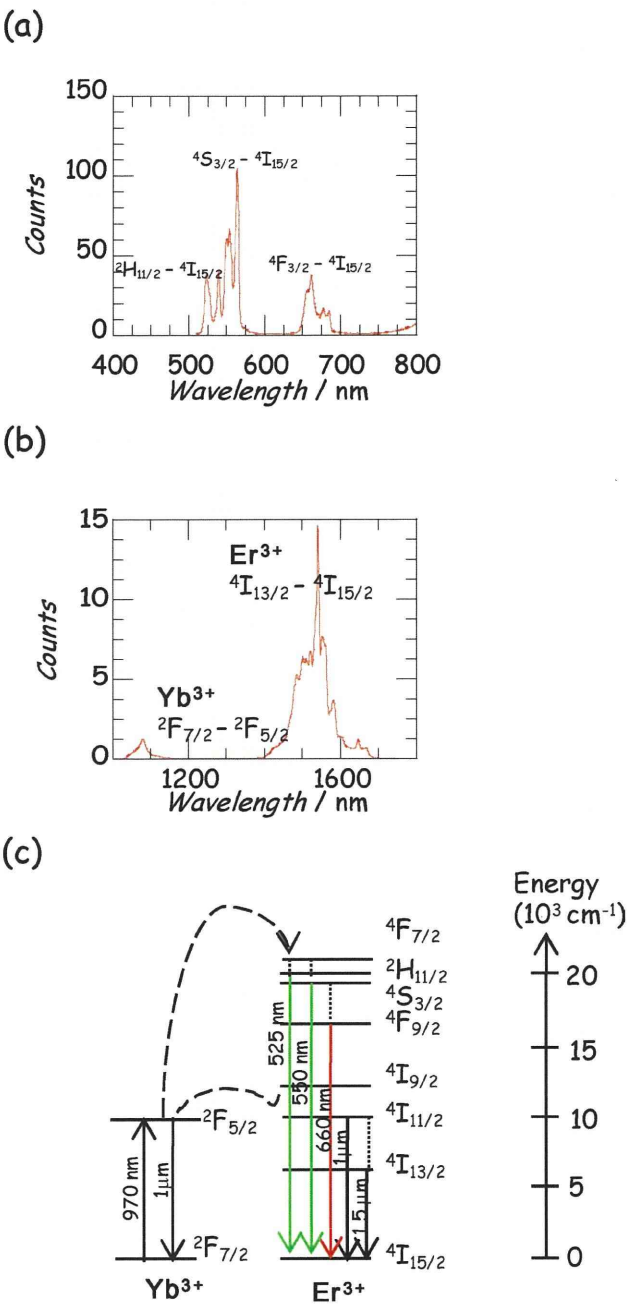

Figure 1. Emission spectra of the RE-NP powder in a) the visible region and b) the NIR region. c) Energy-level diagram of the Yb^{3+} and Er^{3+} system. Full, dashed, and dotted arrows indicate radiative processes, energy transfers, and multiphonon relaxations, respectively.

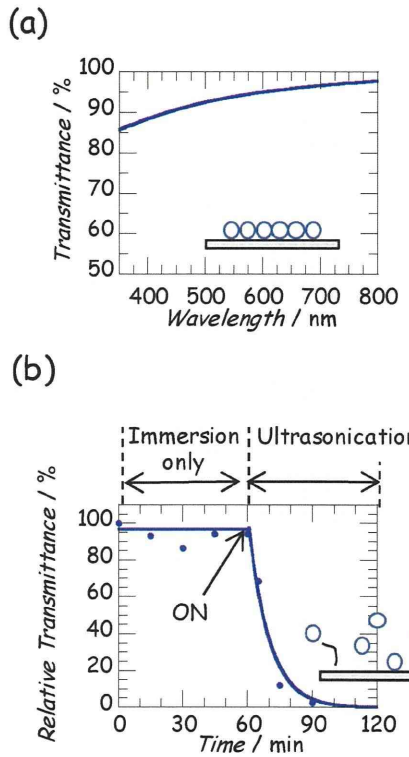

Figure 2. a) Visible transmission spectrum of a RE-NP film dip-coated onto a glass plate. b) Relative transmittance of the RE-NP film at 440 nm as a function of immersion time. The RE-NP film was immersed in acetone for 60 min, followed by ultrasonication in acetone for a subsequent 60 min.

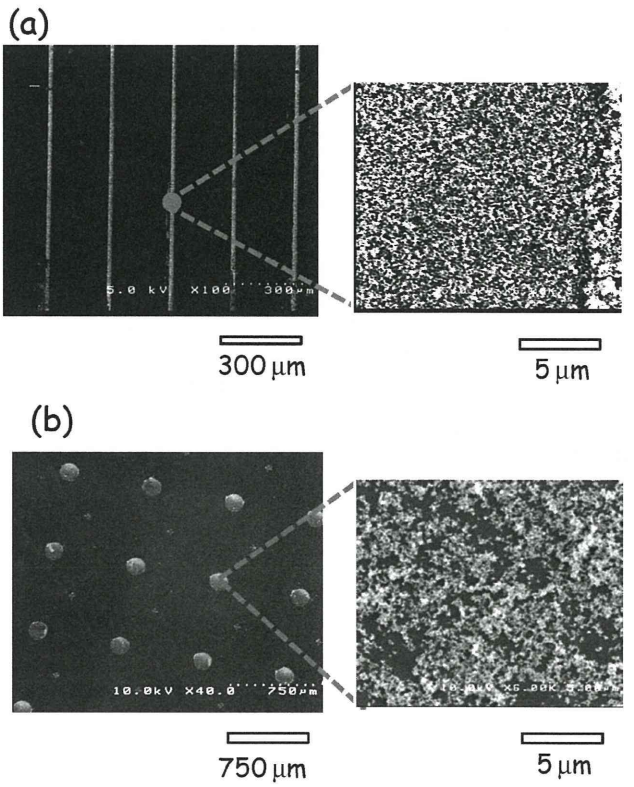

Figure 3. SEM images of RE-NP films dip-coated onto Si wafers patterned by photolithography using photomasks with a) a line pattern and b) a dot pattern.

room temperature. This feature is indispensable for the future applications in sensors, assays, and biology-related fields.

2.2. Surface Patterning of RE-NP Films Using Photolithography

Patterned rare earth ion doped inorganic phosphor films have been fabricated using photolithography[15–18] and soft lithography.[19,20] Etching processes are necessary for the above photolithographic techniques. Etching-free photolithographic techniques that allow for the recycling of inorganic phosphor materials enable us to decrease energy consumption and environmental load.

The stability of the films to immersion in acetone suggests that patterned RE-NP films can be fabricated through lift-off processes in which RE-NP films are first dip-coated on patterned photoresist films, followed by the removal of the photoresist by rinsing in acetone. The desorbed RE-NPs can be easily collected centrifugally from the acetone. We fabricated patterned inorganic phosphor films using the present calcination- and etching-free photolithographic technique (see also Experimental Section and Figure 7).

Figure 3a shows scanning electron microscopy (SEM) images of an RE-NP film with a patterned line structure fthat was fabricated by dip-coating at a dipping speed of 0.1 mm min^{-1}. The line-width of the RE-NP film is 25 μm. The surface of the Si wafer is not exposed in the RE-NP film due to the close packing of RE-NPs as shown in the magnified image of Figure 3a, which indicates the formation of one or more layers of RE-NPs on the deposited region of the Si wafer. Figure 3b shows SEM images of an RE-NP film with a patterned dot structure that was fabricated by dip-coating at a dipping speed of 0.5 mm min^{-1}. Dots with a diameter of 150 μm are evident on the Si wafers. The surface of the Si wafer is exposed between the RE-NPs, which indicates the incomplete formation of a monolayer of RE-NPs, as shown in the magnified image of Figure 3b. These results show that the RE-NP films with designed patterned structures are formed using the present etching-free photolithography. In addition, adjusting the fabrication conditions, such as the dipping speed, enables us to control the thickness and density of the RE-NP films. By using a casting technique, RE-NP films with designed patterns were also fabricated (data not shown).

2.3. Fluorescence and Surface-Potential Imaging of Patterned RE-NP Films

We have demonstrated the fabrication of patterned RE-NP films using etching-free photolithography. RE-NPs are known to show green up-conversion luminescence and NIR fluorescence under irradiation with light at a wavelength of 980 nm. We performed fluorescence imaging of the patterned RE-NP films.

Figure 4a shows an up-conversion fluorescence image of a RE-NP film with a patterned line structure on a glass plate. The image shows green fluorescence from Er^{3+} in the RE-NPs

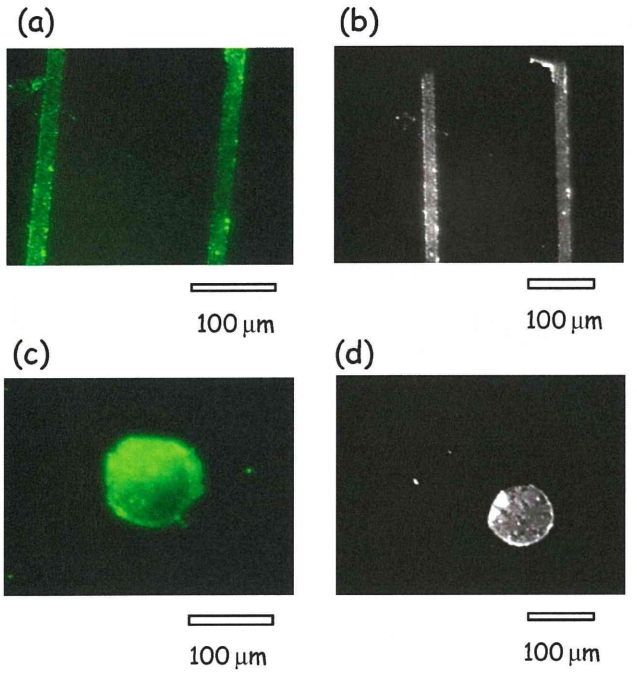

Figure 4. a) Up-conversion fluorescence image and b) NIR fluorescence image of a RE-NP film dip-coated on the glass plate with a patterned line structure. c) Up-conversion fluorescence image and d) NIR fluorescence image of a RE-NP film with a patterned dot structure.

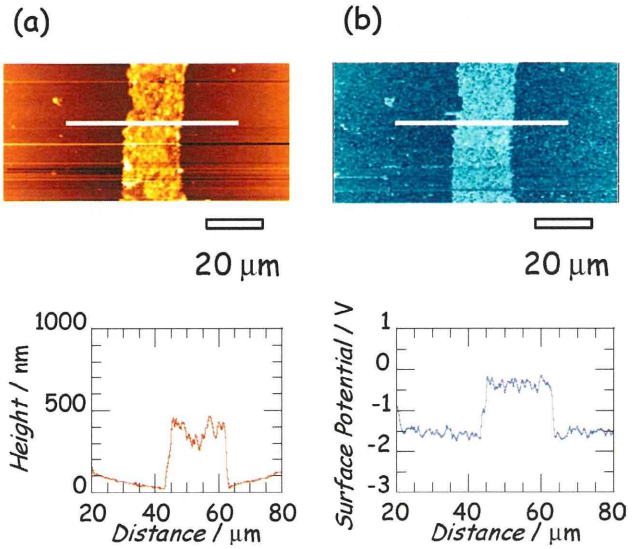

Figure 5. a) AFM image and its cross-sectional view of a RE-NP film dip-coated onto a Si wafer with a patterned line structure. b) Surface-potential image and its profile of the RE-NP film.

at 525 and 560 nm. The line-width in the image is 25 μm, which agrees with that in the SEM images shown in Figure 3a. Figure 4b shows an NIR fluorescence image of the RE-NP film. The image shows NIR fluorescence from Er^{3+} and Yb^{3+} in the RE-NPs at around 1500 and 1100 nm. Figure 4c shows an up-conversion fluorescence image of a RE-NP film with a patterned dot structure. The image shows green fluorescence from Er^{3+} in the RE-NPs at 525 and 560 nm. The diameter of the dot in the image is 80 μm, which coincides with that in the SEM image shown in Figure 3b. Figure 4d shows an NIR fluorescence image of the RE-NP film. The image shows NIR fluorescence from Er^{3+} and Yb^{3+} in the RE-NPs at around 1500 and 1100 nm, respectively. These results demonstrate that the RE-NP films with designed patterned structures serve as inorganic phosphors in the visible and NIR regions.

Scanning Kelvin probe force microscopy (KPFM) enables us to investigate local work-function distribution of surfaces of various materials such as metals[23] and organic semiconductors.[24] Considering that Y_2O_3 in the RE-NPs and native SiO_2 on the Si wafers have different work functions, we performed atomic force microscopy (AFM) and KPFM observations to study the local material distribution of the patterned RE-NP films.

Figure 5a shows an AFM image and its cross-sectional view of an RE-NP film with a patterned line structure on an Si wafer. The thickness of the RE-NP film is about 500 nm. These results suggest the formation of double -ayer films of RE-NPs, taking into account that the diameter of the RE-NPs is about 280 nm (see Experimental Section). The line-width is about 25 μm, which agrees with those obtained from SEM observation and fluorescence imaging. Figure 5b shows a KPFM image and corresponding profile of the RE-NP film. The surface potential of the RE-NP film is larger than that of the Si wafer by about 1.5 V. Surface potential reflects the work function of the material. The work function of the matrix Y_2O_3 in the RE-NPs is ca. 2.0 eV,[25] and that of native SiO_2 on the Si wafer is 3.0–3.4 eV.[26] The difference between the surface potentials of the two regions observed in the KPFM measurements is consistent with the difference between the work function of the two materials. These results demonstrate that the RE-NP films are selectively formed in the designed region using calcination- and etching-free photolithography. AFM observations also reveal the formation of double layers of the RE-NPs in the films.

2.4. Photolithography of RE-NP Films on Plastic Sheets

Soft lithography, when employed to fabricate patterned inorganic phosphor films without etching processes, requires the calcination of the precursors of the inorganic phosphor films after patterning them onto solid substrates. New techniques without calcination processes will be indispensable for the fabrication of patterned inorganic phosphor films as functional materials have been fabricated on flexible substrates in many fields.[21] We fabricated patterned RE-NP films onto flexible substrates such as PET sheets using our calcination-free technique.

Figure 6a shows an optical microscopic image of an RE-NP film dip-coated onto a PET sheet with a patterned line structure. The line-width of the RE-NP film is 25 μm. Agglomerated RE-NPs are present in some parts of the lines. The sizes of the agglomerated RE-NPs are several micrometers. Figure 6b shows an up-conversion florescence image of the RE-NP film with a patterned line structure. The image shows green fluorescence from Er^{3+} in the RE-NPs at 525 and 560 nm. Figure 6c shows a NIR florescence image of the RE-NP film with a patterned line structure. The image shows NIR fluorescence from Er^{3+} and Yb^{3+} in the RE-NPs at around 1100 and 1500 nm, respectively.

ADVANCED FUNCTIONAL MATERIALS
www.afm-journal.de

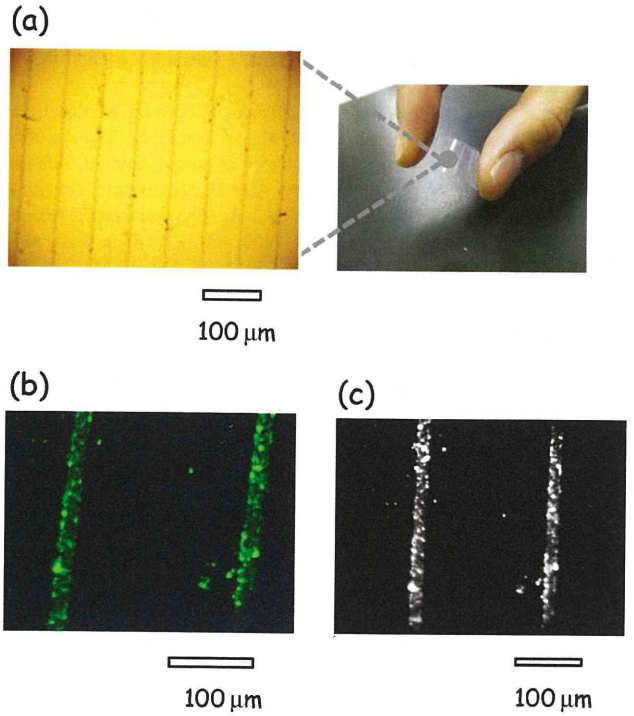

Figure 6. a) Optical microscopic image and photograph, b) visible up-conversion luminescence image, and c) NIR fluorescence image of a RE-NP film dip-coated onto a PET sheet with a patterned line structure.

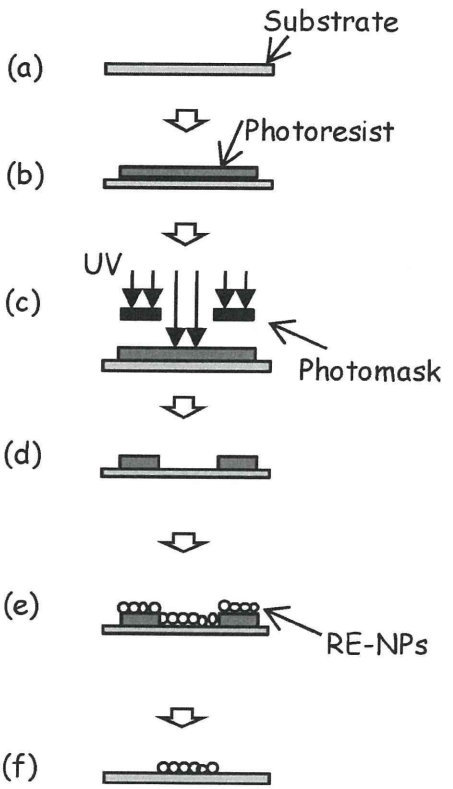

Figure 7. Scheme of calcination- and etching-free photolithography of RE-NP films fabricated by dip-coating; a) cleaning the substrates, b) application of photoresist films, c) UV exposure through photomasks, d) development, e) deposition of RE-NP films by dip-coating, and f) lift-off.

These results demonstrate that the RE-NP films with designed patterned structures on flexible substrates serve as inorganic phosphor films in the visible and NIR regions. Further, the optimization of the fabrication conditions, such as the concentration of the RE-NP solution and dip-coating speed, will be necessary to increase the homogeneity of the RE-NP films.

3. Conclusions

In this study, we have demonstrated that our calcination- and etching-free photolithography enables us to fabricate patterned inorganic phosphor films consisting of fluorescent RE-NPs. The visible transmittance of the RE-NP films is more than 90%, and is comparable to that of inorganic phosphor films fabricated by the combination of sol-gel method and soft lithography.[19,20]

The present methodology is free from calcination and etching processes and allows the fabrication of patterned inorganic films on flexible substrates. In addition, RE-NPs can be easily collected centrifugally after the lift-off processes, which indicates that the patterning can be performed at low cost and material consumption. The present methodology is versatile in that it can be applied to low phonon materials other than Y_2O_3 as host material and to various substrates. The present methodology will find wide application to the fabrication of inorganic phosphor films for use in various flexible devices in the future. The immobilization of RE-NPs on the patterns through covalent bonding will further increase the potential of this methodology; we are currently working along this line.

4. Experimental Section

Materials: $Y(NO_3)_3$, $Er(NO_3)_3{\cdot}5H_2O$, and $Yb(NO_3)_3{\cdot}5H_2O$ used for the preparation of RE-NPs were purchased from Aldrich. 10 mol L^{-1} urea aqueous solution was purchased from Kanto Chemical Corporation. Acetone and chloroform used for cleaning the substrates were purchased from Wako Pure Chem. Ind., Ltd. The photoresist of Az 1500 and its developer were purchased from MicroChemicals.

Fabrication of RE-NPs: RE-NPs were synthesized using the recipe of Venkatachalam et al.[9b] Precursor solution was prepared by adding 8 mmol $Y(NO_3)_3$, 0.08 mmol $Er(NO_3)_3{\cdot}5H_2O$, and 0.06 mmol $Yb(NO_3)_3$ $5H_2O$ into 40 mL 10 mol L^{-1} urea aqueous solution. 10 mL water was added to the precursor solution under stirring. The precursor solution was kept at 98 °C in a water bath for 1 h. The obtained precursor powder was washed centrifugally three times with distilled water, dried at 80 °C, and then calcinated at 900 °C for 30 min. The diameter of the RE-NPs was estimated to be about 280 nm using dynamic light scattering.

Cleaning of Substrates: Glass plates, n-type Si wafers with native oxide (resistivity 1–10 Ω cm), and PET sheets used as the substrates were rinsed with acetone and then with chloroform under ultrasonication for 20 min each. After drying with nitrogen gas, the substrates were irradiated with UV light from a low-pressure mercury lamp for 15 min in an ozone atmosphere generated from a PL 16-110 ultraviolet-ozone cleaner (Sen Lights Corp., Japan). The distance between the substrates and the light source was about 5 cm. (**Figure 7**a)

Fabrication of Patterned RE-NP Films by Dip-Coating: After the substrates were cleaned, a solution of Az 1500 photoresist was spin-coated onto the substrates, first at a rotational speed of 1000 rpm for 10 s, and then at 3000 rpm for 30 s. The photoresist films were kept at 100 °C for 5 min in an N_2 atmosphere for drying (Figure 7b), followed by UV exposure for 10–15 s from a 100-W high pressure Hg lamp through a photomask

consisting of vapor-deposited Cr films on a quartz substrate. Two types of photomasks were used; one with a line pattern with line/space of 15/200 (μm/μm) and the other with a pattern of dots with diameters of 100 and 140 μm (Figure 7c). The photoresist films were immersed in the developer solution with gentle shaking for 30 s and rinsed three or four times with distilled water, which resulted in the formation of patterned photoresist films on the substrates (Figure 7d). 1 mg mL^{-1} RE-NPs in water was ultrasonicated for 1 h at room temperature before use for thorough dispersion of the RE-NPs in water. RE-NP films were deposited on the patterned substrates using dip-coating at a dipping speed of 0.1 to 0.5 mm s^{-1} (Figure 7e). Then, the samples were immersed and gently shaken in acetone for 30 s, which resulted in the selective removal of the photoresist films and the RE-NPs adsorbed on them (Figure 7f).

Characterization: Visible emission spectra were measured with RF-5000 (Shimadzu, Japan). NIR emission spectra were obtained with an NIR spectrometer (AvaSpec, USA) and a semiconductor laser diode at 980 nm. Transmission spectra were measured with a V-560 (JASCO, Japan). Fluorescence imaging was carried out with an IX-71 (Olympus, Japan) attached to a band-path filter at a wavelength of 550 nm, and a ion-pass filter at a wavelength of 1000 nm. AFM and KPFM observations were performed with an SPA 300 AFM unit with a Nanonavi controller (SII nanotechnology, Japan). The measurements were made in noncontact mode using an Au-coated Si tip with a resonance frequency of 27 kHz and a spring constant of 1.7 N m^{-1}. AC voltage was applied to the cantilever at a voltage of 10 V, which oscillated at a resonance frequency of 26 kHz.

Acknowledgements

This work was partly supported by the Japan Society for the Promotion of Science (Grant No. 22850017).

Received: March 31, 2011
Revised: May 9, 2011
Published online: September 23, 2011

[1] a) S. Horiuchi, T. Fujita, T. Hayakawa, Y. Nakao, *Adv. Mater.* **2003**, *15*, 1449; b) D. Öner, T. J. McCarthy, *Langmuir* **2000**, *16*, 7777; c) M. D. Levenson, N. S. Viswanathan, R. A. Simpson, *IEEE Trans. Electron. Dev.* **1982**, *29*, 1828; d) E. W. H. Jager, E. Smela, O. Inganäs, *Science* **2000**, *290*, 1540; e) A. S. Blawas, W. M. Reichert, *Biomaterials* **1998**, *19*, 595.

[2] a) B. D. Myers, C. P. Dravid, *Nano Lett.* **2006**, *6*, 963; b) J. I. Martin, J. Nogues, K. Liu, J. L. Vicent, I. K. Schuller, *J. Magn. Magn. Mater.* **2003**, *256*, 449; c) T. H. P. Chang, *J. Vac. Sci. Technol.* **1975**, *12*, 1271.

[3] a) A. Kumar, H. A. Biebuyck, G. M. Whitesides, *Langmuir* **1994**, *10*, 1498; b) Y. Xia, G. M. Whitesides, *Annu. Rev. Mater. Sci.* **1998**, *28*, 153; c) M. A. Unger, H. Chou, T. Thorsen, A. Scherer, S. R. Quake, *Science* **2000**, *288*, 113; d) G. M. Whitesides, E. Ostuni, S. Takayama, X. Jiang, D. E. Ingber, *Annu. Rev. Biomed. Eng.* **2001**, *3*, 335; e) M. Cavallini, C. Albonetti, F. Biscarini, *Adv. Mater.* **2009**, *21*, 1043.

[4] a) R. D. Piner, J. Zhu, F. Xu, S. Hong, C. A. Mirkin, *Science* **1999**, *283*, 661; b) D. S. Ginger, H. Zhang, C. A. Mirkin, *Angew. Chem. Int. Ed.* **2004**, *43*, 30; c) K. Salaita, Y. Wang, C. A. Mirkin, *Nature Nanotech.* **2007**, *2*, 145; d) Y. Li, B. W. Maynor, J. Liu, *J. Am. Chem. Soc.* **2001**, *123*, 2105.

[5] a) S. Krämer, R. R. Fuierer, C. B. Gorman, *Chem. Rev.* **2003**, *103*, 4367; b) A. Naber, H. Kock, H. Fuchs, *Scanning* **1996**, *18*, 567; c) M. M. Alkaisi, R. J. Blaikie, S. J. McNab, R. Cheung, D. R. S. Cumming, *Appl. Phys. Lett.* **1999**, *75*, 3560; d) S. Sun, G. J. Leggett, *Nano Lett.* **2004**, *4*, 1381.

[6] a) W. A. Lopes, H. M. Jaeger, *Nature* **2001**, *414*, 735; b) R. A. Segalaman, *Mater. Sci. Eng. Rep.* **2005**, *48*, 191; c) C. Tang, E. M. Lennon, G. H. Fredrickson, E. J. Kramer, C. J. Hawker, *Science* **2008**, *322*, 429; d) H. Mattoussi, L. H. Radzilowski, B. O. Dabbousi, D. E. Fogg, R. R. Schrock, E. L. Thomas, M. F. Rubner, M. G. Bawendi, *J. Appl. Phys.* **1999**, *86*, 4390; e) M. Cavallini, J. Gomez-Segura, C. Albonetti, D. Ruiz-Molina, J. Veciana, F. Biscarini, *J. Phys. Chem. B* **2006**, *110*, 11607.

[7] a) M. Matsumoto, S. Watanabe, K. Tanaka, H. Kimura, M. Kasahara, H. Shibata, R. Azumi, H. Sakai, M. Abe, Y. Kondo, N. Yoshino, *Adv. Mater.* **2007**, *19*, 3668; b) S. Watanabe, H. Kimura, T. Sato, H. Shibata, F. Sakamoto, R. Azumi, H. Sakai, M. Abe, M. Matsumoto, *Langmuir* **2008**, *24*, 8735; c) S. Watanabe, H. Shibata, F. Sakamoto, R. Azumi, H. Sakai, M. Abe, *J. Mater. Chem.* **2009**, *19*, 6796; d) S. Watanabe, H. Shibata, H. Horiuchi, R. Azumi, H. Sakai, M. Abe, M. Matsumoto, *J. Colloid Interface Sci.* **2010**, *343*, 324; e) M. Matsumoto, K. Tanaka, R. Azumi, Y. Kondo, N. Yoshino, *Langmuir* **2004**, *20*, 8728; f) H. Shibata, M. Sato, S. Watanabe, M. Matsumoto, *Colloid Surface A* **2009**, *346*, 58.

[8] a) M. Gleiche, L. F. Chi, H. Fuchs, *Nature* **2000**, *403*, 173; b) O. Purrucker, A. Förtig, K. Lüdtke, R. Jordan, M. Tanaka, *J. Am. Chem. Soc.* **2005**, *127*, 1258; c) N. Lu, M. Gleiche, J. Zheng, S. Lenhert, B. Xu, L. Chi, H. Fuchs, *Adv. Mater.* **2002**, *14*, 1812; d) N. Lu, X. Chen, D. Molenda, A. Naber, H. Fuchs, D. V. Talapin, H. Weller, J. Muller, J. M. Lupton, J. Feldmann, A. L. Rogach, L. Chi, *Nano Lett.* **2004**, *4*, 885.

[9] a) G. Mialon, S. Türkcan, G. Dantelle, D. P. Collins, M. Hadjipanayi, R. A. Taylor, T. Gacoin, A. Alexandrou, J. P Boilot, *J. Phys. Chem. C* **2010**, *114*, 22449; b) N. Venkatachalam, Y. Saito, K. Soga, *J. Am. Ceram. Soc.* **2009**, *92*, 1006.

[10] T. Konishi, M. Yamada, K. Soga, D. Matsuura, Y. Nagasaki, *J. Photopolym. Sci. Technol.* **2006**, *19*, 145.

[11] S. V. Eliseeva, J. G. Bünzli, *Chem. Soc. Rev.* **2010**, *39*, 189.

[12] B. H. Cumpston, S. P. Ananthavel, S. Barlow, D. L. Dyer, J. E. Ehrlich, L. L. Erskine, A. A. Heikal, S. M. Kuebler, I. Y. Sandy Lee, D. McCord-Maughon, J. Qin, H. Röckel, M. Rumi, X. Wu, S. R. Marder, J. W. Perry, *Nature* **1999**, *398*, 51.

[13] M. J. Miller, S. H. Wei, I. Parker, M. D. Cahalan, *Science* **2002**, *296*, 1869.

[14] D. Matsuura, *Appl. Phys. Lett.* **2002**, *81*, 4526.

[15] E. Sluzky, K. Hesse, *J. Electrochem. Soc.* **1989**, *126*, 2742.

[16] P. J. Holmes, R. G. Loasby, in *Handbook of Thick Film Technology*; Electrochemical Publications, Ayr, UK, **1976**, p 50.

[17] J. E. Jang, J. H. Gwak, Y. W. Jin, S. J. Lee, H. Park, J. E. Jung, N. S. Lee, *J. Vac. Sci. Technol. B* **2000**, *18*, 1106.

[18] Y. W. Jin, J. E. Jang, W. K. Yi, J. E. Jung, N. S. Lee, J. M. Kim, D. Y. Jun, J. P. Hong, *J. Vac. Sci. Technol. B* **1999**, *17*, 489.

[19] a) M. Yu, J. Lin, Z. Wang, J. Fu, S. Wang, H. J. Zhang, Y. C. Han, *Chem. Mater.* **2002**, *14*, 2224; b) M. Yu, J. Lin, J. Fu, H. J. Zhang, Y. C. Han, *J. Mater. Chem.* **2003**, *13*, 1413.

[20] a) W. Wang, Z. Cheng, P. Yang, Z. Hou, C. Li, G. Li, Y. Dai, J. Lin, *Adv. Funct. Mater.* **2011**, *21*, 456; b) M. L. Pang, J. Lin, Z. Y. Cheng, J. Fu, R. B. Xing, S. B. Wang, *Mater. Sci. Eng. B* **2003**, *100*, 124; c) M. L. Pang, J. Lin, J. Fu, R. B. Xing, C. X. Luo, Y. C. Han, *Opt. Mater.* **2003**, *23*, 547.

[21] a) S. Zhang, Y. Shen, H. Fang, S. Xu, J. Song, Z. L. Wang, *J. Mater. Chem.* **2010**, *20*, 10606; b) J. C. Ribierre, T. Fujiwara, S. Watanabe, M. Matsumoto, T. Muto, A. Nakao, T. Aoyama, *Adv. Mater.* **2010**, *22*, 1; c) S. R. Forrest, *Nature* **2004**, *428*, 911.

[22] a) D. R. Gamelin, H. U. Güdel, *Top. Curr. Chem.* **2001**, *214*, 1; b) F. Auzel, *Chem. Rev.* **2004**, *104*, 139.

[23] V. Palermo, M. Palma, P Samori, *Adv. Mater.* **2006**, *18*, 145.

[24] a) H. Hoppe, T. Glatzel, M. Niggemann, A. Hinsch, M. C. Lux-Steiner, N. S. Sariciftci, *Nano Lett.* **2005**, *5*, 269; b) S. Watanabe, T. Aoyama, Y. Fukuchi, T. Yamashita, M. Matsumoto, T. Wada, *J. Photopolym. Sci. Technol.* **2009**, *22*, 571.

[25] K. Koumoto, W. S. Seo, S. Ozawa, *Appl. Phys. Lett.* **1997**, *71*, 1475.

[26] H. E. Romero, H. Shen, P. Joshi, H. R. Gutierrez, S. A. Tadigadapa, J. O. Sofo, P. C. Eklund, *ACS Nano* **2008**, *2*, 2037.

journal

J. Am. Ceram. Soc., 94 [10] 3301–3307 (2011)
DOI: 10.1111/j.1551-2916.2011.04583.x

Low-Temperature Spark Plasma Sintering of Yttria Ceramics with Ultrafine Grain Size

Hidehiro Yoshida,[*,†,‡] Koji Morita,[*,‡] Byung-Nam Kim,[‡] Keijiro Hiraga,[*,‡] Kohei Yamanaka,[§] Kohei Soga,[*,§] and Takahisa Yamamoto[*,¶]

[‡]Nano Ceramics Center, National Institute for Material Science, Ibaraki 305-0047, Japan

[§]Department of Materials Science and Technology, Tokyo University of Science, Chiba 278-8510, Japan

[¶]Department of Advanced Materials Science, The University of Tokyo, Chiba 277-8561, Japan

The sinterability of high-purity, nanocrystalline Y_2O_3 without any additives was investigated by spark plasma sintering (SPS) for a combination of low sintering temperatures (850°–1050°C) and low heating rates (2–50°C/min). At a sintering temperature of 950°C and a heating rate of 2°C/min, the SPS yielded a polycrystalline Y_2O_3 having a relative density of 99% and an average grain size of 190 nm. The Y_2O_3 bodies sintered at 950° and 1050°C for 1h at the heating rate of 2°C/min exhibited an in-line transmittance of 6%–46% in a wavelength range of 400–800 nm. A high-resolution transmission electron microscopy observation and chemical analysis by an energy-dispersive X-ray spectrometer revealed that the sintered Y_2O_3 bodies were single-phase materials without any grain-boundary amorphous layer or impurity contamination. An isothermal SPS experiment indicated that the grain-boundary mobility is significantly enhanced by the SPS. An electron energy loss spectrometry indicated that SPS changed atomic configuration of the grain boundaries. The improved sinterability of Y_2O_3 is attributed to the enhanced diffusion that arises from defect reactions activated by the SPS.

I. Introduction

YTTRIA (Y_2O_3) is a promising material for refractory/optical applications because of its high corrosion resistivity,[1] thermal stability,[2] wide optical transmission range[3,4] and high melting point of around 2410°C.[5,6] A significant number of sintering methods have been developed to obtain dense Y_2O_3 polycrystals, and fully densified Y_2O_3 has been successfully obtained by hot-press sintering,[7–9] hydrogen atmosphere sintering[10] and vacuum sintering.[11–14] Conventional techniques for the fabrication of dense Y_2O_3 polycrystals, however, need very high sintering temperatures (typically >1600°C) and/or sintering aids.

Another available technique for fabricating densified Y_2O_3 is spark plasma sintering (SPS). SPS processing has been widely used to sinter dense and fine-grained ceramics,[15,16] and has been recently applied to the sintering of Y_2O_3.[17,18] We have recently examined the sinterability of undoped, nanocrystalline Y_2O_3 powders by SPS at the sintering temperatures between 650° and 1050°C, and showed that dense Y_2O_3 with a relative density >97% can be prepared by low-temperature SPS at a sintering temperature of 850°C.[17] In addition, our previous studies on SPS have revealed that a low heating rate is highly efficient for the fabrication of fine-grained, transparent Al_2O_3[19] and $MgAl_2O_4$.[20] The present study aims to optimize SPS conditions for densification of Y_2O_3 at temperatures lt;1100°C, and to examine influence of SPS on high-temperature matter transport in Y_2O_3. For this purpose, we examined heating rate dependence of densification in Y_2O_3, and investigated microstructure by high-resolution transmission electron microscopy (HRTEM) and electron energy-loss spectroscopy.

II. Experimental Procedure

The starting material in this study was commercially available, high-purity Y_2O_3 powder (BB-type; Shin-Etsu Rare Earth, Tokyo, Japan) with a manufacturer-determined average particle size of 20 nm and a BET multipoint specific surface area of 37.0 m^2/g. Table I lists the impurities from the manufacturer's certificate of analysis. The as-received Y_2O_3 powder was ball milled with zirconia balls in ethanol for 24 h, dried and then sifted through a 60-mesh sieve for granulation. The ball-milling and granulation processes were necessary to load the powder into the carbon die for SPS due to the poor flowability of the raw powder. No contamination of the sintered Y_2O_3 from the zirconia balls was detected using an energy-dispersive X-ray spectrometer (EDS) attached to a transmission electron microscope (to be described in Section III).

Using a SPS machine (SPS-1050; Sumitomo Coal Mining, Kawasaki, Japan), the granulated powder was heated to the desired sintering temperature under vacuum (about 10^{-1} Pa) and at a uniaxial compressive pressure of 80 MPa in a carbon die having an inside diameter of 12 mm. The present materials were sintered at a sintering temperature from 850° to 1050°C for 1 h. The samples were heated at a constant heating rate from room temperature to the sintering temperature, and the heating rate ranged from 2 to 50°C/min. The temperature was measured by a thermocouple attached to a nonthrough hole (1 mm diameter and 5 mm depth) in the side of the carbon die. The carbon die was covered with carbon heat insulation to avoid heat dissipation from the external surface of the die. In addition, for comparison of electron energy-loss spectroscopy analyses (to be described), dense Y_2O_3 polycrystals sintered in air or in a vacuum were prepared as follows. The granulated Y_2O_3 powders were cold-isostatically pressed at 120 MPa, and the green compacts were then sintered in air or in a vacuum (about 10^{-1} Pa) at 1700°C for 3 h without pressure. The heating rate was 5°C/min, and fully densified materials were obtained.

An isothermal SPS experiment was also performed in order to examine the grain growth behavior during SPS. The granulated powder was heated under the above-described conditions at the

A. Zangvil—contributing editor

Manuscript No. 28298. Received July 9, 2010; approved March 27, 2011.

A part of this study was supported by a Grant-in-Aid for Scientific Research (B) 21360328, a Grant-in-Aid for Scientific Research (C) 22560674, and a Grant-in-Aid for Scientific Research on Priority Areas 474-19053008 from the JSPS and the Ministry of Education, Culture, Sports, Science and Technology (MEXT), Japan. This study was also supported by the World Premier International Research Center Initiative (WPI Initiative), MEXT, Japan.

*Member, The American Ceramics Society.

†Author to whom correspondence should be addressed. e-mail: YOSHIDA.Hidehiro@nims.go.jp

Table I. Impurities in Commercial Y_2O_3 Powder (from the Manufacturer's Certificate of Analysis)

Element	CaO	Fe_2O_3	Dy_2O_3	Ho_2O_3	Er_2O_3	Yb_2O_3
Maximum impurities (ppm)	10	5	30	30	30	30

heating rate of 2°C/min from room temperature to 950° or 1050°C, and the temperature was then maintained for 0–8 h.

The in-line transmittance was measured in the wavelength range from 240 to 1200 nm using a double-beam spectrophotometer (SolidSpec-3700DUV; Shimadzu, Tokyo, Japan). The distance between the sample and the detector was about 55cm. For the measurement, the sintered body was mirror-polished on both sides to a final thickness of 1 mm using a diamond slurry.

The densities of the sintered compacts were measured by Archimedes method. The theoretical density of Y_2O_3 has been reported to be 5.03 g/cm^3.[21] The microstructure of the present specimens was characterized by scanning electron microscopy (SEM, SU-8000; Hitachi, Tokyo, Japan) and HRTEM (EM-002BF; Topcon, Tokyo, Japan). The average grain sizes of the present materials were evaluated using an average diameter of >300 grains in the SEM photographs of the fractured surfaces; in the materials sintered by SPS, grain-boundary grooves were not formed by thermal etching at <1000°C in air. The TEM specimens were prepared using standard techniques involving mechanical grinding to a thickness of <0.1 mm, and ion beam milling to an electron transparency at about 4 kV. Chemical analysis was performed by an EDS (Voyager, Noran Instruments, Middleton, WI) attached to the HRTEM using a probe size of about 1 nm. Electron energy loss spectrometry (EELS; Enfina spectrometer, Gatan, Pleasanton, CA) measurements were carried out in the HRTEM at 12 different grain boundaries and grain interiors in three specimens, namely, the Y_2O_3 sintered by SPS at 950° and 50°C/min, the Y_2O_3 sintered at 1700°C in a vacuum, and the Y_2O_3 sintered at 1700°C in air. The probe size was about 1 nm. The full-width at half-maximum of the zero-loss peak was 1.2 eV under the present conditions, and the energy resolution of the EELS was 0.2 eV.

III. Experimental Results

Figure 1 shows the relative density of the Y_2O_3 bodies obtained by SPS for each heating rate as a function of the sintering temperature. The relative density of the present materials is >94%, and the relative density of 99% is achieved at the sintering temperatures of 950° and 1050°C and the heating rate of 2°C/min. The present sintering temperature is significantly lower than that required for the fabrication of dense Y_2O_3 using the conventional sintering; a sintering temperature of 1600°C was required to achieve a relative density of 98% through pressureless sintering in air by using the same Y_2O_3 nanocrystalline powder.[17] The relative density of the present materials increased with the increasing sintering temperature and decreasing heating rate; for instance, at the sintering temperature of 1050°C, the relative density is 95% at the heating rate of 50°C/min and 99% at 2°C/min. Under the present sintering conditions, a high sintering temperature and a lower heating rate result in a higher density Y_2O_3.

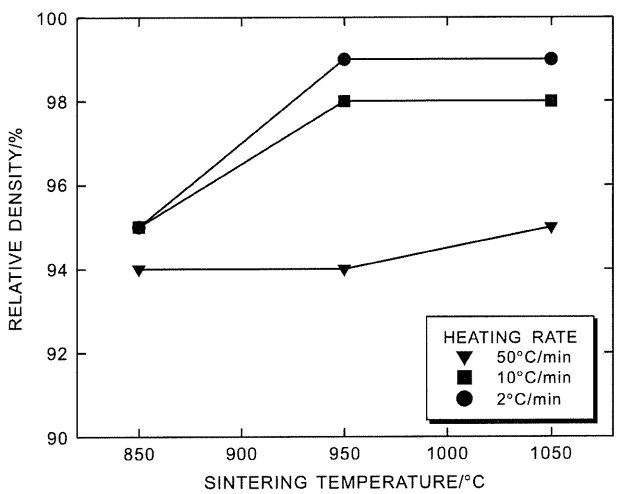

Fig. 1. Relative density of Y_2O_3 fabricated by SPS as a function of sintering temperature for heating rate in the range from 2 to 50°C/min.

Figure 2 shows SEM micrographs of the fracture surfaces of Y_2O_3 fabricated at the sintering temperatures of 850°, 950°, and 1050°C and at the heating rates of 2, 10, and 50°C/min. The fracture surfaces exhibited homogeneous microstructures with equiaxed polyhedral grains. The Y_2O_3 bodies sintered at 950° and 1050°C at 2°C/min exhibited a nearly fully densified structure with small pores having diameters of about 10–20 nm, while relatively large pores with diameters of about 100–200 nm can be seen at some multiple junctions of the materials sintered at 950° and 1050°C and heating rates of 10 and 50°C/min. This observation is consistent with the relative density (Fig. 1); the low heating rate contributes to eliminating residual pores and consequently increasing the relative density.

Figure 3 shows the average grain size for each heating rate as a function of the sintering temperature. The grain size increases with increasing sintering temperature and decreasing heating rate. For instance, at the sintering temperature of 950°C, the grain size is 0.67 μm at the heating rate of 50°C/min, but decreases to 0.19 μm at 2°C/min. Low heating rates during SPS result in smaller grain sizes in Y_2O_3.

The present materials with the relative density of 99% exhibit a translucency at a visible wavelength. Figure 4 shows the in-line transmittance for the wavelength of light in the Y_2O_3 bodies sintered at 950° and 1050°C for 1 h at the heating rate of 2°C/min. The thicknesses of the specimens were 1 mm. The Y_2O_3 sintered at 1050°C exhibits the in-line transmittance of 6%–46% in the wavelength range of 400–800 nm.

Figure 5 shows the average grain sizes of the Y_2O_3 bodies at 950° and 1050°C as a function of isothermal holding time during SPS. The grain size increased with the increasing holding time. Because the relative density of the Y_2O_3 bodies sintered at 950° and 1050°C for 0 h was 98%, influence of the residual pores on the grain growth can be neglected. The grain growth rate in single-phase ceramics usually obeys a rate equation for normal grain growth,[22,23]

$$d^2 - d_0^2 = K(t - t_0) \tag{1}$$

where d_0 is the reference grain size at time t_0, d is the average grain size at time t and K is the growth constant. The value of K is usually given as $2M\gamma$ where M is the grain-boundary mobility and γ is the grain-boundary energy. It has been reported that the static grain growth in micrometer/submicrometer grained Y_2O_3 can be well described by the parabolic law of Eq. (1) under pressureless annealing in air and under vacuum in the temperatures range of 1500°–1650°C.[24] Figure 6(a) is a plot of $d^2 - d_0^2$ versus the isothermal holding time $t - t_0$ at 950° and 1050°C. The square of the grain size versus the annealing time exhibited a single straight line for each material, and the value of the proportionality constant K can be obtained from the slope of the lines. The grain-boundary mobility was evaluated to be 2.0×10^{-17} m$^4 \cdot$(J·s)$^{-1}$ at 950°C and 8.5×10^{-17} m$^4 \cdot$(J·s)$^{-1}$ at 1050°C by assuming $\gamma = 0.3$ J/m^2.[24] Figure 6(b) shows an Arrhenius plot of the grain-boundary mobility at 950° and 1050°C. The activation energy for the grain-boundary mobility determined from the slope of the Arrhenius plot was 194 kJ/mol.

Figure 7 shows a typical HRTEM image of a multiple junction in the Y_2O_3 sintered at 950°C and at the heating rate of

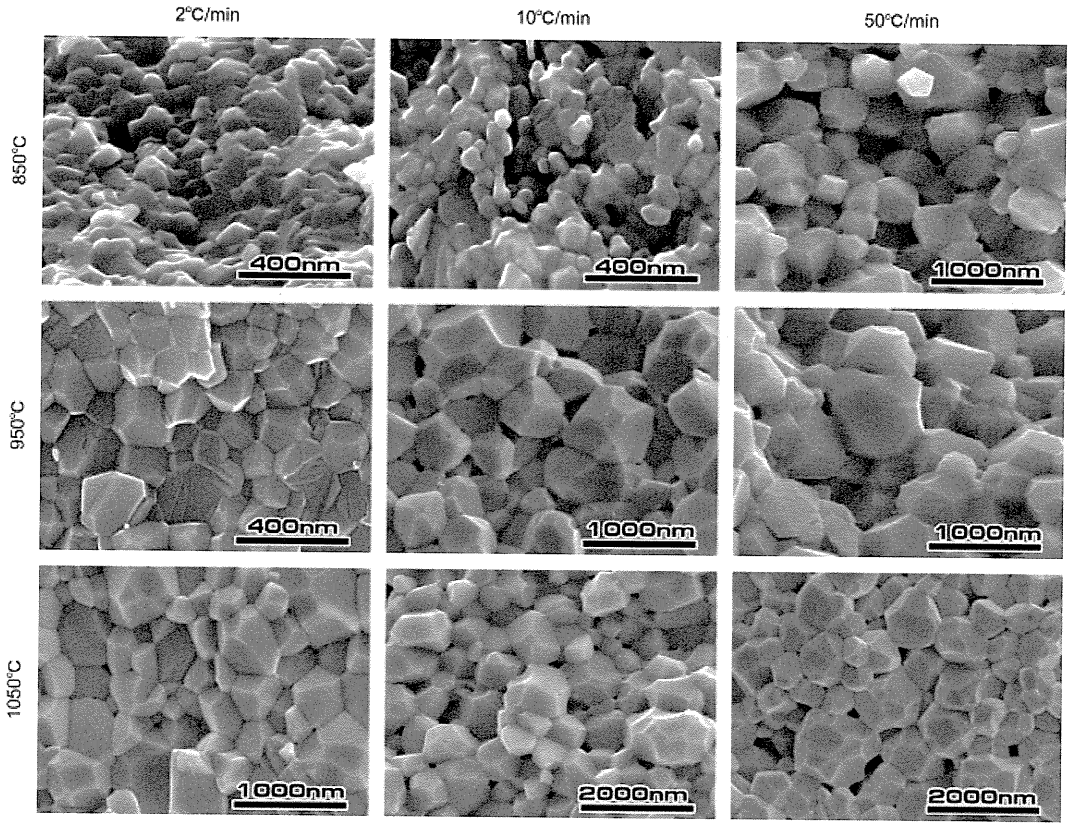

Fig. 2. SEM micrographs of fracture surfaces of Y_2O_3 sintered at 850°, 950°, and 1050°C (in the first, second, and third row, respectively) and at the heating rate of 2, 10, and 50°C/min (in the first, second, and third column, respectively).

50°C/min. The lattice fringes can be seen for the three grains, and neither an amorphous layer nor second phase particle is observed along the grain boundaries; the grains are directly bonded for each other at the boundaries. As typically shown in Fig. 7, the present specimens sintered by SPS exhibit a single-phase microstructure. This result indicates that the densification during the SPS proceeds by solid-state sintering.

Figure 8 shows typical nanoprobe EDS spectra acquired from a grain interior, a grain boundary and a multiple junction in Y_2O_3 sintered at 950°C and the heating rate of 50°C/min. The peaks identified as Cu at 8.1 and 8.9 keV originated from the TEM specimen holder. The peaks from yttrium, carbon and oxygen are observed in the three spectra, and no other element (such as zirconium) signals were detected. This result indicates that the sintered Y_2O_3 was free of impurities due to the granulation and sintering processes, and that the improved sinterability of Y_2O_3 by SPS is not attributed to impurity effects.

Figure 9(a) shows a typical *O–K* near-edge profile (ELNES) taken from the grain boundary (black line) and grain interior (gray line) in Y_2O_3 sintered by SPS at 950 and 10°C/min. For comparison, the *O–K* edges for the Y_2O_3 bodies pressureless-sintered under vacuum and in air at 1700 and 5°C/min are shown in Figs. 9(b) and (c), respectively. All of the spectra exhibit two peaks (labeled α and β in Fig. 9) at the energy-loss level of about 533 and 537 eV. The shape of the oxygen *K*-edge in Y_2O_3 has also been reported in the literature,[25,26]

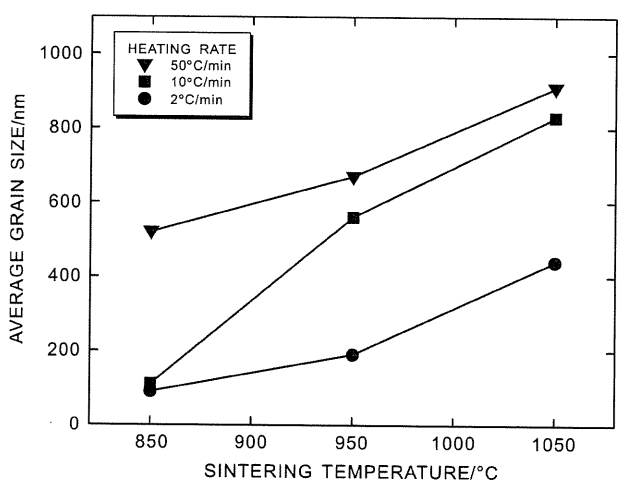

Fig. 3. Average grain size of Y_2O_3 fabricated by SPS as a function of sintering temperature for heating rates in the range from 2 to 50°C/min.

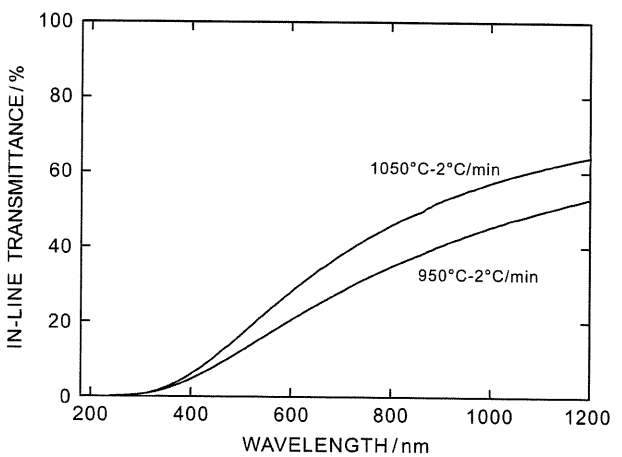

Fig. 4. In-line transmittance of Y_2O_3 bodies sintered at 950° and 1050°C for 1 h at the heating rate of 2°C/min. The sample thickness is 1 mm.

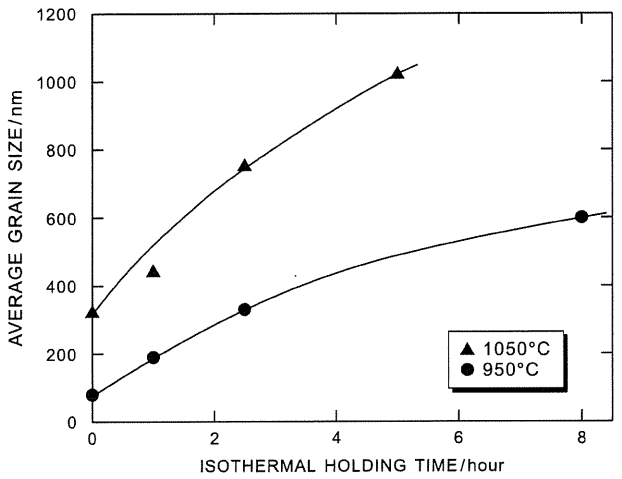

Fig. 5. Average grain size of Y_2O_3 bodies at 950° and 1050°C as a function of the isothermal holding time.

and the presence of the two peaks is explained from the tetrahedral arrangement of the oxygen atoms in Y_2O_3.[27] All the spectra obtained from the three specimens are essentially identical. However, the intensity ratio of peak α to peak β depends on the sintering condition and on the analysis point. In the spectrum for the specimen sintered in air (Fig. 9(c)), the spectra of the grain interior and grain boundary are almost identical, and the intensity of peak α is higher than peak β. In the spectrum for the vacuum-sintered specimen (Fig. 9(b)), the intensity of peak α is slightly higher than that of peak β in the grain interior, but the intensity of peak α is slightly lower than peak β at the grain boundary. On the other hand, in the spectrum for the SPS specimen (Fig. 9(a)), the intensity of peak α is nearly the same as that of peak β in the grain interior. In addition, the intensity of peak α is relatively lower than the intensity of peak β

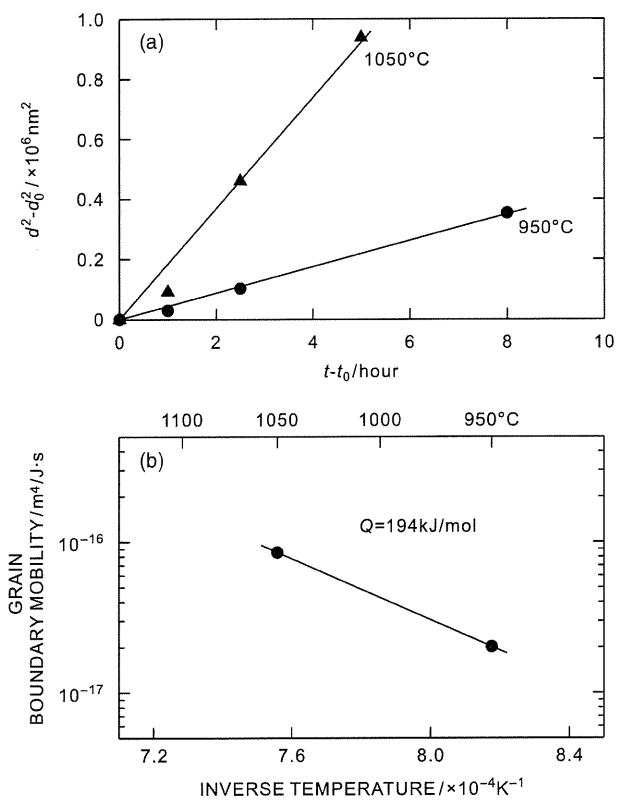

Fig. 6. (a) A plot of $d^2 - d_0^2$ as a function of the holding time $t-t_0$ at 950° and 1050°C. (b) An Arrhenius plot of the grain-boundary mobility at 950° and 1050°C.

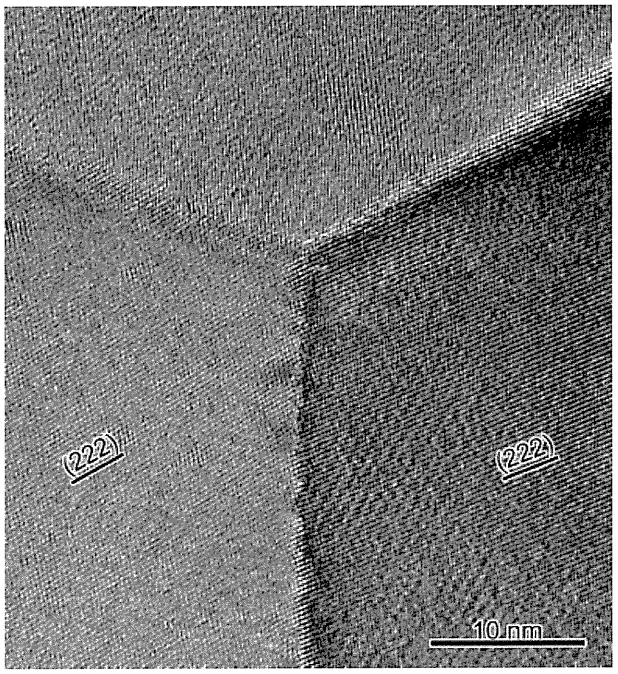

Fig. 7. A high-resolution transmission electron microscopy image in the vicinity of a multiple junction of Y_2O_3 sintered at 950°C and the heating rate of 50°C/min.

at the grain boundary. Because yttrium with a valence configuration of $4d^15s^2$ usually has only the 3+ oxidation state in solid materials,[28] the difference in the spectra is attributed to the difference in atomic configuration rather than the difference in ionic valence. The present ELNES analysis revealed the following points. First, the atomic configuration of Y_2O_3 is influenced by the vacuum sintering, and is sensitively influenced by SPS in comparison with the pressureless sintering in air. Second, SPS significantly influenced the grain-boundary atomic configuration in comparison with that of the grain interior.

IV. Discussion

(1) Microstructure

In the present study, polycrystalline Y_2O_3 with a relative density >99% is obtained by SPS at the sintering temperature of 950°

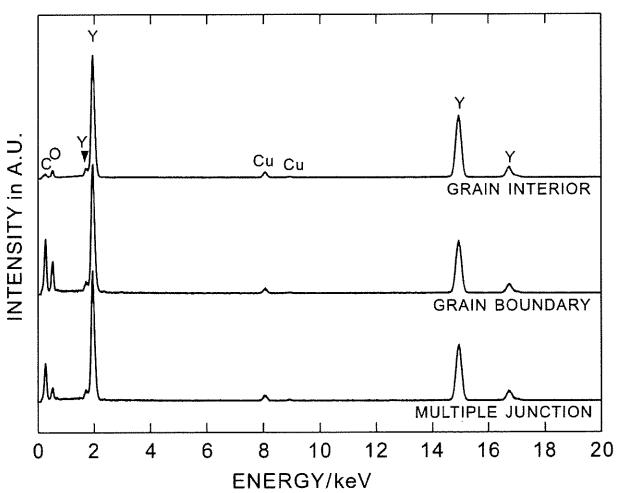

Fig. 8. Typical energy-dispersive X-ray spectroscopy spectra acquired at a grain interior, a grain boundary and a multiple junction in Y_2O_3 sintered at 950°C and a heating rate of 50°C/min. The probe size was about 1 nm.

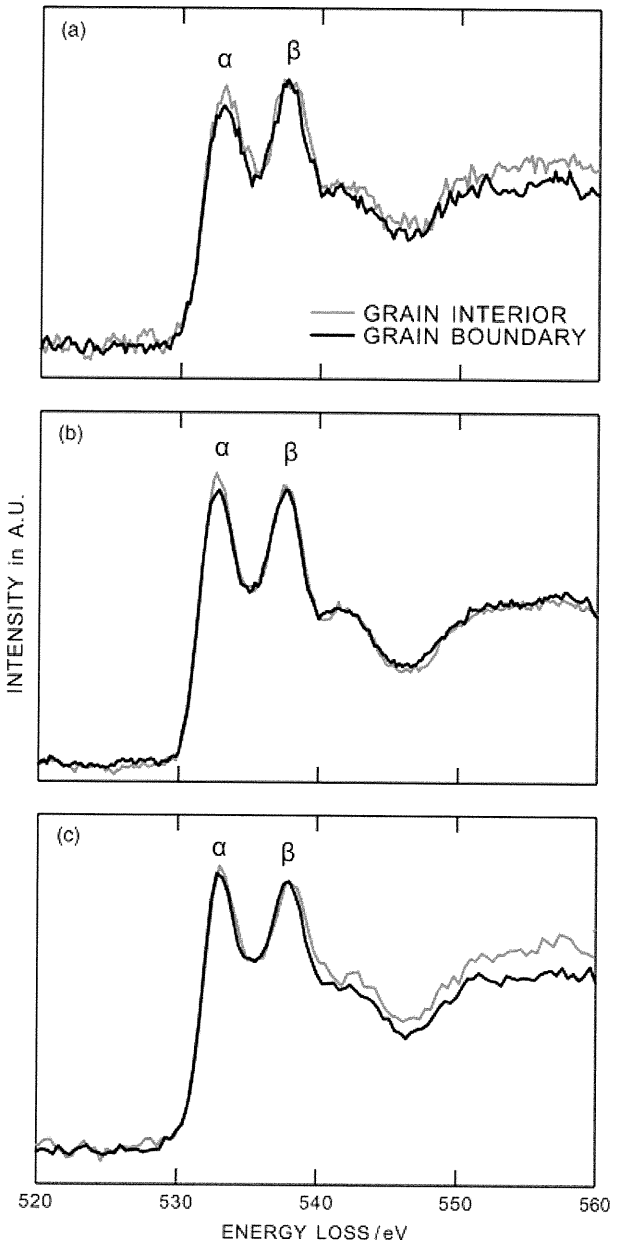

Fig. 9. *O–K* ELNESs acquired at grain boundary and grain interior in (a) Y_2O_3 sintered by SPS at 950° and 10°C/min, (b) Y_2O_3 sintered in a vacuum at 1700° and 5°C/min, and (c) Y_2O_3 sintered in air at 1700° and 5°C/min.

or 1050°C and the heating rate of 2°C/min. The average grain sizes of the Y_2O_3 bodies sintered at 950° and 1050°C are 190 and 440 nm, respectively. In addition, the dense Y_2O_3 bodies exhibit a translucency at the visible wavelength. On the other hand, Chaim *et al.*[18] has examined the SPS of Y_2O_3 in the sintering temperature range of 1100°–1600°C at the heating rates between 50 and 180°C/min, and they reported that dense Y_2O_3 with the average grain size of 4 μm was fabricated by SPS at 1400°C and the heating rate of 180°C/min. The SPS with the combination of a relatively low sintering temperature and heating rate is efficient for the fabrication of dense, nanocrystalline Y_2O_3.

In the present study, the lower heating rates result in not only a higher relative density, but also a smaller grain size. Chaim *et al.*[18] reported that the higher heating rate of SPS yields a higher relative density in Y_2O_3. The present result is opposite to their report. In fact, according to widely accepted recognition, fast heating is efficient for enhancing densification and retarding grain growth during conventional sintering of oxide ceramics.[29] The causes of the higher relative densities and smaller grain sizes at the lower heating rates during SPS have not yet been clarified. However, this is not a special phenomenon limited to the present material, but has been reported in Al_2O_3[19,30] and $MgAl_2O_4$[20] after SPS.

Murayama and Shin[31] investigated the effects of heating rate on densification and grain growth in hot-pressed alumina. Their results indicated that a rapid heating rate yielded a larger grain size; after sintering at 1250°C for 4 min, the grain sizes of alumina were about 0.42 and 0.55 μm at heating rates of 5 and 500°C/min, respectively. For the reason of the larger grain size at the higher heating rate, Murayama and Shin explained by assuming that a high defect concentration is produced by rapid heating. During SPS, high DC current for attaining rapid heating may assist defect formation owing to high-temperature plasma generated on particle surfaces. In addition, SPS involves such a plastic deformation as grain-boundary sliding.[15,32] The deformation may induce defects which can cause dynamic grain growth.[33,34] The defect produced by both the heating and deformation may therefore accelerate the grain growth during SPS at a high heating rate.

As shown in Fig. 2, the compacts sintered at the heating rate of 50°C/min included relatively large pores with diameters of about 100–200 nm at some multiple junctions, while the compacts sintered at 2°C/min included small pores with diameters of about 10–20 nm. During a final stage of sintering, it is known that pores become isolated at grain corners, and grain growth and densification simultaneously proceed.[35] For a given level of intergranular porosity, coalesced pores yield a limited effect of dragging on grain growth and inhibit full-densification in comparison with the case of small, isolated pores. At higher heating rates, pore coalescence is possible during an intermediate stage of sintering where pore channels along multiple grain junctions become isolated at grain corners.[35] At low heating rates, on the other hand, pores homogeneously dispersed at multiple junctions may effectively suppress grain growth of Y_2O_3 during the final stage of SPS.

For the enhanced densification for the smaller grain size, the following explanation is possible. Since a smaller grain size means a larger value of grain-boundary area per unit volume and hence a larger value of the total flux of grain-boundary diffusion, the smaller grain size should enhance total matter transport by grain-boundary diffusion. In addition, the smaller grain size must facilitate grain-boundary sliding during SPS.[15,32]

Further detailed investigation of the microstructure, such as grain size and pore size, is desirable in order to elucidate the development of the microstructure during SPS and to clarify the mechanism of enhanced densification and suppressed grain growth at lower heating rates.

(2) Kinetics of Grain-Boundary Mobility

The present value of M is comparable to the previously reported data for Y_2O_3 at 1500°C.[24] According to the previous report,[24] the grain-boundary mobility in undoped Y_2O_3 was about 1.7×10^{-17} $m^4 \cdot (J \cdot s)^{-1}$ in air and 9.9×10^{-17} $m^4 \cdot (J \cdot s)^{-1}$ in a reduced atmosphere at 1500°C. The data indicate that SPS has an effect equivalent to an increase in the sintering temperature by about 500°C. The reported values of the activation energy for grain-boundary mobility in Y_2O_3[24,36] are listed in Table II. The reported values of the activation energy for M were obtained by pressureless annealing in air[24] or in a vacuum.[36] The activation energy for the grain-boundary mobility in the present study (194 kJ/mol) is significantly lower than those reported previously.

The activation energy for the grain-boundary migration is usually comparable to the activation energy for the diffusion of the rate-controlling ion species. Several types of mass transport experiments have been done to measure the diffusion coefficient in single crystals[37–39] and polycrystals[40,41] of Y_2O_3. A partial list of the activation energies for the diffusion coefficient in Y_2O_3 is given in Table III. The activation energy for oxygen anion's